An-Najah National University

Faculty of Graduate Studies

SPECTROCHEMICAL CHARACTERIZATION OF AN ELECTRON TRANSFER MINIATURIZED PROTEIN SCAFFOLD MIMICS RUBREDOXIN METAL SITE: MOLYBDENUM – MINIATURIZED ELECTRON TRANSFER PROTEIN-SINGLE CHAIN 1 (MO-METPSC1)

By

Rafeef Mohammad Abd Al-Majeed Odwan

Supervisors

Dr. Diaa Aref

Dr. Mohammed Suleiman

This Thesis is Submitted in Partial Fulfillment of the Requirements for The Degree of Master of Chemistry, Faculty of Graduate Studies, An Najah National University, Nablus-Palestine.

2024

SPECTROCHEMICAL CHARACTERIZATION OF AN ELECTRON TRANSFER MINIATURIZED PROTEIN SCAFFOLD MIMICS RUBREDOXIN METAL SITE: MOLYBDENUM – MINIATURIZED ELECTRON TRANSFER PROTEIN-SINGLE CHAIN 1 (MO-METPSC1)

By
Rafeef Mohammad Abd Al-Majeed Odwan

This thesis was Defended successfully on 12/10/2024, and approved by:

Dr. Diaa Aref Supervisor	Signature
Dr. Mohammed Suleiman Co-Supervisor	Signature
Dr. Huseein Alkam External Examiner	Signature
Dr. Rawan Khalaf Internal Examiner	Signature

Dedication

I dedicate this research to the students of Gaza and to all those whose dreams have not yet been fulfilled and remain hostage to the rubble of homes, under a sky filled with smoke.

To the spirits of the martyrs, to the resistance, you are the teachers of this generation, and to you all its work.

Acknowledgement

Completing this thesis has been a collaborative journey, and I am deeply grateful to the many individuals who supported me along the way.

My deepest appreciation goes to my thesis supervisors, Dr. Diaa Aref, and Dr. Muhammad Suleiman, and special thanks to Dr. Marco Chino. Their combined expertise provided invaluable guidance throughout the research process.

I would also like to express my sincere gratitude to the Artificial Metallo-Enzymes Group (AMEG) at Federico II University, Italy, for their warm hospitality and invaluable support during my research stay. Their expertise and guidance were instrumental in shaping my research and enhancing my understanding of my research.

I am also deeply grateful to Erasmus+ (KA171) for providing me with the Erasmus+ grant scholarship, which allowed me to pursue this research opportunity in Italy. This experience has been truly enriching, both academically and personally.

On a personal level, I owe a debt of gratitude to my family and friends. Their unwavering support, particularly my mother, provided me with the strength and motivation to persevere during challenging moments.

Declaration

I, the undersigned, declare that I submitted the thesis entitled:

SPECTROCHEMICAL CHARACTERIZATION OF AN ELECTRON TRANSFER MINIATURIZED PROTEIN SCAFFOLD MIMICS RUBREDOXIN METAL SITE: MOLYBDENUM – MINIATURIZED ELECTRON TRANSFER PROTEIN-SINGLE CHAIN 1 (MO-METPSC1)

I declare that the work provided in this thesis, unless otherwise referenced, is the researcher's own work, and has not been submitted elsewhere for any other degree or qualification.

Student's Name: Rafeef Mohammad Odwan

Signature: Rafeef

Date: 12/10/2024

List of Contents

List of Tables

List of Figures

List of Scheme

List of Appendixes

SPECTROCHEMICAL CHARACTERIZATION OF AN ELECTRON TRANSFER MINIATURIZED PROTEIN SCAFFOLD MIMICS RUBREDOXIN METAL SITE: MOLYBDENUM – MINIATURIZED ELECTRON TRANSFER PROTEIN-SINGLE CHAIN 1 (MO-METPSC1)

By
Rafeef Mohammad Abd Al-Majeed Odwan
Supervisors
Dr. Diaa Aref
Dr. Mohammed Suleiman

Abstract

Metal atoms are crucial in catalysis and are integral to the structure and function of many enzymes and proteins. A primary goal in protein design is to develop small, stable, and simple peptide scaffolds that can replicate the catalytic activity of complex protein metal centers. These artificial mimics have significant potential in areas such as environmental applications, biotechnology, and fundamental research.

In this study, we focused on the Miniaturized Electron Transfer Protein single chain 1 (METPsc1) peptide, reconstituted to mimic a rubredoxin-like metal-binding site with a precise tetrathiolate environment. The reconstitution of the Molybdenum-Miniaturized Electron Transfer Protein single chain 1 (Mo-METPsc1) peptide was achieved using varying peptide-to-metal ratios. It was characterized through multiple spectroscopic techniques, including UV-Vis, Circular Dichroism (CD), and Magnetic Circular Dichroism (MCD) spectroscopy.

UV-vis spectroscopy identified two broad absorption bands, with peaks between 310-330 nm and 420-460 nm, indicating successful incorporation of molybdenum into the tetrathiolate environment. CD spectroscopy provided additional confirmation of molybdenum binding, evidenced by a positive band at 394 nm. MCD spectroscopy, which is sensitive to electronic structure and oxidation state, revealed that the molybdenum in the metal-binding site is in the $^{+}6$ oxidation state (Mo (VI)).

Those spectroscopic analyses support molybdenum's successful incorporation and functionality within the peptide scaffold. To further investigate the reduction capabilities of the Mo-METPsc1 complex, reduction studies were conducted using dithionate and

dithiothreitol (DTT) as substrates. Spectroscopic analysis following these tests demonstrated the compound's catalytic activity in reducing the dithionate molecule.

Keywords: Artificial Metallopeptidase; Biocatalysis; METPsc1; Molybdenum-binding peptides; Rubredoxin

Chapter One

Introduction

1.1 Metalloprotein

Metals play an essential role in biological systems, owing to their diverse reactivity profiles exhibited by their complexes. Such as in biological processes of cellular respiration, photosynthesis, and safeguarding against toxic substances [1]. Within biological systems, metal ions are primarily managed and transported by proteins, ensuring their accessibility for various biological functions.

Metalloproteins are a class of proteins that comprise one or more metal centers. [2], which can be of the same or different types. These metal centers form bonds with donor atoms on the side chains of proteins or non-protein cofactors.

The metal center in a metalloprotein essentially serves two crucial roles:

1. Structural Role: It influences the protein's adoption of a specific three-dimensional structure.
2. Functional Role: It actively participates in the protein's biological function.

Both the immediate binding environment and the protein matrix itself significantly shape the functionality of a metalloprotein. Factors such as hydrophobicity, charge density, and hydrogen bonding interactions between neighboring ions play a vital role in this influence [3].

Consequently, modulating the proteins' function is possible by modifying the chemical environment surrounding the ion. In metalloproteins incorporating transition metals, the shape, number, and symmetry properties of the d orbitals directly contribute to the diverse spectroscopic, magnetic, and catalytic characteristics observed for these metalloproteins, and the nature of their bonds can vary from highly electrostatic to highly covalent [4].

On the other hand, Ligands are a set of atoms or negatively charged molecules that form bonds with a metal ion. These ligands act as electron-pair donors according to Lewis's

base theory. They can be categorized as monodentate or polydentate upon their electron-pair donation properties to the metal ion.

In metalloproteins, ligands that bind to metal ions typically originate from the polypeptide chain and are referred to as endogenous ligands. There are only a few amino acids that commonly participate in coordination within "the metal-binding sites" of these proteins [5]. The most prevalent coordinating amino acids include glutamic acid (Glu), cysteine (Cys), histidine (His), and aspartic acid (Asp), which mainly coordinate through their side chains containing oxygen, sulfur, or nitrogen electron-donor atoms. Other amino acids are less frequently involved in metal coordination [6].

The preferences of metal ions for specific amino acid side chains align with the principles of coordination chemistry, often explained by the hard and soft acids and bases (HSAB) theory. Besides endogenous ligands, metal ions can also coordinate with exogenous cofactors, which are ligands not derived from the polypeptide chain. These exogenous ligands include small inorganic molecules like hydroxides, oxides, and water, as well as organic macrocyclic ligands such as corrins, porphyrins, and chlorins [7].

These ligands collectively form the first coordination sphere around each metal ion, often referred to as prosthetic groups. Prosthetic groups can be categorized into five fundamental types based on their specific functions:

1. Structural: Stabilize the protein's tertiary or quaternary structure [8].
2. Storage: Involved in the acquisition, binding, and release of metals in a soluble form [8].
3. "Electron Transfer": Facilitate the uptake, release, and storage of electrons [8].
4. "Dioxygen Binding": Enable the reversible binding of metal ions with oxygen (O_2) [8].
5. Catalytic: Participate in substrate binding, activation, and catalysis [8].

The coordination in metalloproteins can also be understood through the concept of concentric spheres: the first coordination (inner) sphere consists of atoms directly interacting with the metal ion, while the second coordination sphere includes atoms that

interact with the ligands in the inner sphere. The number of atoms involved in these spheres depends on the size of both the metal ion and the ligand atoms, with four and six being the most common coordination numbers in metalloproteins [9,10].

In biological systems (i.e. enzymes), the metalloproteins play a vital role in their active sites, aiding the regulation of their function. The Metal ions contribute to the binding of substrates, swift formation of the transition state, and facilitate the products' release [11, 12]. In an enzyme's active site, the distribution of charges is purposefully arranged to stabilize the transition state of the catalyzed reaction concerning the substrate. In enzyme-catalyzed reactions, the precise spatial orientation of the reactants is crucial; otherwise, the likelihood of the reaction occurring diminishes, leading to lower reaction rates. The electrostatic environment within the active site plays a significant role in directing the substrate toward the binding site in the correct orientation.

1.2 Electron Transfer Proteins

In nature, energy acquisition occurs via the electron transfer (ET) process, where electrons are extracted from the fuel, and subsequently flow towards an oxidizing agent along a potential gradient formed by a sequence of acceptor/donor units in a so-called respiratory chain [2]. Significant fuels encompass sugars, fats, and molecular hydrogen (H_2). While the biological oxidants include oxygen (O_2), nitrate (NO_3^-), and protons (H^+).

In the realm of biology, a relatively limited set of redox-active metal ions is employed to facilitate this electron transfer chain. Metalloproteins emerge as the predominant electron transfer centers within biology, and they can be categorized into three primary classes: Cytochromes, iron-sulfur (FeS) proteins, and cupredoxins that comprise "type 1 copper (T_1Cu) proteins and CuA centers" [13,14].

Each ET protein class can facilitate the electron exchange between various redox partners, with distinct reduction potentials (E°). Consequently, the ET centers must adapt their E° to align with those of respective redox partners. These three protein classes collectively span the physiological E°, which extends from -1V to 1V, corresponding to the protons' reduced form (H_2) and water oxidation to O_2, respectively. Cupredoxins operate at the

higher end of the E° range, while the E° of FeS proteins notably overlaps with that of cytochromes, which possess intermediate E° values [14]. Typically, these enzymes are embedded within a membrane, where the energy derived from electron transfer (ET) is harnessed in establishing a gradient of protons across the membrane.

1.2.1 Cytochromes

Many years ago, researchers first identified cytochromes as cellular pigments [10]. Cytochromes are a type of enzyme composed of an Iron-porphyrin prosthetic group; they utilize the low spin configuration of iron couple states (Fe^{3+}/Fe^{2+}). The iron ions in Cytochromes are hexacoordinated, where five of the coordination sites are provided by the porphyrin and protein binding residue, and the remaining (6^{th}) coordination site is either vacant or occupied by exogenous molecules (i.e. H_2O molecule) [10].

1.2.2 Iron-Sulfur (FeS) Proteins

"Iron-sulfur (FeS) proteins" are one of the oldest metalloproteins found on Earth, which are characterized by forming clusters of primarily four iron metals and four sulfur atoms [14]. In Early life forms, organisms utilized the redox properties of the FeS clusters as essential redox centers [14]. Later on, when the environment became more oxidizing, FeS proteins continued to serve as vital electron carriers [15].

FeS clusters are categorized based on the number of iron and sulfur atoms within the cluster. Additionally, FeS centers can be classified according to the type of protein they are associated with, including rubredoxins, ferredoxins, and others that are summarized in (Table 1.1).

Each class of FeS proteins exhibits a common structural motif, and the metal cofactor within them adopts a distorted tetrahedral geometry. In most FeS proteins, each iron atom is surrounded by four ligands. Among the most common ligands are cysteine amino acids or inorganic sulfur atoms.

In biological systems, FeS clusters exhibit remarkable efficiency in facilitating rapid electron transfer, which arises from their ability to distribute the added electron to

different extents. This distribution minimizes changes in bond lengths and decreases the reorganization energy, a phenomenon referred to as the "entatic effect." In complex enzymatic structures, such that in hydrogenases, the FeS clusters are arranged in a relay-like configuration that facilitates efficient long-range electron transfer between distant redox-active sites within its entity [16].

In almost all instances, the iron (Fe) ions exhibit tetrahedral coordination with the thiolate cysteine amino acid ligand. Nevertheless, in other instances, one or more Fe ions can be bounded by non-thiolate amino acid ligands, like carboxylates, imidazoles, or alkoxyls (like serine), or other exogenous ligands.

Table 1.1

Classification of FeS proteins

Cluster	Class	Structure	Redox state	UV-vis (nm)	Transition	Isomer shift (mms^{-1})	Total Spin
1Fe	Rubredoxin		$Fe^{2+/3+}$	311, 331, reduced *Cp*Rd; 350, 380, oxidized *Cp*Rd; 490 , 570, 750, oxidized *D. gigas* Rd;	Fe^{2+}	0.7	2
					Fe^{3+}	0.32	5/2
2Fe-2S	Ferredoxin	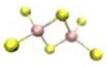	$[2Fe\text{-}2S]^{1+/2+}$	330,420, 436, 560,oxidized	$Fe^{3+}Fe^{2+}$	0.35, 0.65	1/2
				312, 350,390,540, oxidized	$2Fe^{3+}$	0.27	0
	Rieske	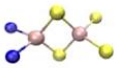	$[2Fe\text{-}2S]^{1+/2+}$	325, 458, shoulder at 560 -580 (oxidized)	$Fe^{3+}Fe^{2+}$	0.35, 0.65	1/2
				380-383, 425-433,505-550 (reduced)	$2Fe^{3+}$	0.27	0
3Fe-4S	Ferredoxin	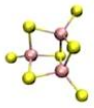	$[3Fe\text{-}4S]^{0/1+}$	Broad absorption at 380-400	$2Fe^{2.5+}1Fe^{3+}$	0.46.0.32	2
					$3Fe^{3+}$	0.27	1/2
4Fe-4S	Ferredoxin		$[4Fe\text{-}4S]^{1+/2+}$	Broad absorption at 380-400	$2Fe^{2+}2Fe^{2.5+}$	3/2, 0.5, 0.58	1/2
					$4Fe^{2.5+}$	0.42	0
	HiPIP		$[4Fe\text{-}4S]^{2+/3+}$	388, shoulder at 450 and 735	$4Fe^{2.5+}$	0.42	0
					$2Fe^{2.5+}2Fe^{3+}$	0.4, 0.29	1/2

The FeS centers exhibit negative reduction potentials, usually falling below -0.2 V. Consequently, their reduced forms function as effective reducing agents. There are exceptions, such as HiPIP centers, which operate between the $^{+}3$ and $^{+}2$ oxidation states, and Rieske centers, represented by "[2Fe-2S] clusters" with one Fe site coordinated by

two neutral imidazole ligands rather than cysteine. Coordination by histidine stabilizes the iron as Fe(II) and often elevates the reduction potential to a significantly more positive value, surpassing +0.2 V [17]. This is essential for its functional as an electron carrier and plays key roles in enzyme active sites, including reducing disulfide bonds, initiating or stabilizing radical chain reactions, and acting as Lewis acids. They also provide structural stability to proteins and can store sulfur and iron [17–19].

1.3 Rubredoxins (Rds)

Rubredoxins (Rds) are a class of FeS proteins characterized by their simplicity. Typically, they are small proteins consisting of approximately 45-54 amino acids with a molar mass ranging from 6-7 kDa. They are predominantly found in bacteria, archaea, and anaerobic organisms. At their core, they feature a mono-iron center surrounded by four cysteines arranged in "two Cys-$(Xxx)_2$-Cys-Gly segments", adopting a distorted tetrahedral geometry (Scheme 1.1) [14].

Among the family of rubredoxins, one of the most extensively studied members is "the rubredoxin" extracted from the mesophilic bacterium Clostridium pasteurianum (CpRd) [14]. Conversely, rubredoxin extracted from the hyperthermophilic archaeon Pyrococcus furiosus (PfRd) stands out for its exceptional thermal stability "melting temperature of 200 °C" [20,21].

The primary structure of rubredoxin forms "a three-strand antiparallel β-sheet", constituting the protein's overall fold [14]. This arrangement encompasses a hydrophobic core and displays a pseudo-2-fold symmetry. Within this structure, conserved aromatic residues, combined with a specific set of bulky aliphatic residues (such as Ile/Leu/Val33), play a role in stabilizing the three-dimensional structure of the protein [14]. Additionally, this configuration aids in excluding water molecules from accessing the metal center within the protein [17].

Scheme 1.1

Overall Fold of Chain (a) of CpRd (PDB ID: 1IRO). (b) NH–·SH Bond around the $Fe(Cys)_4$ Center [14]

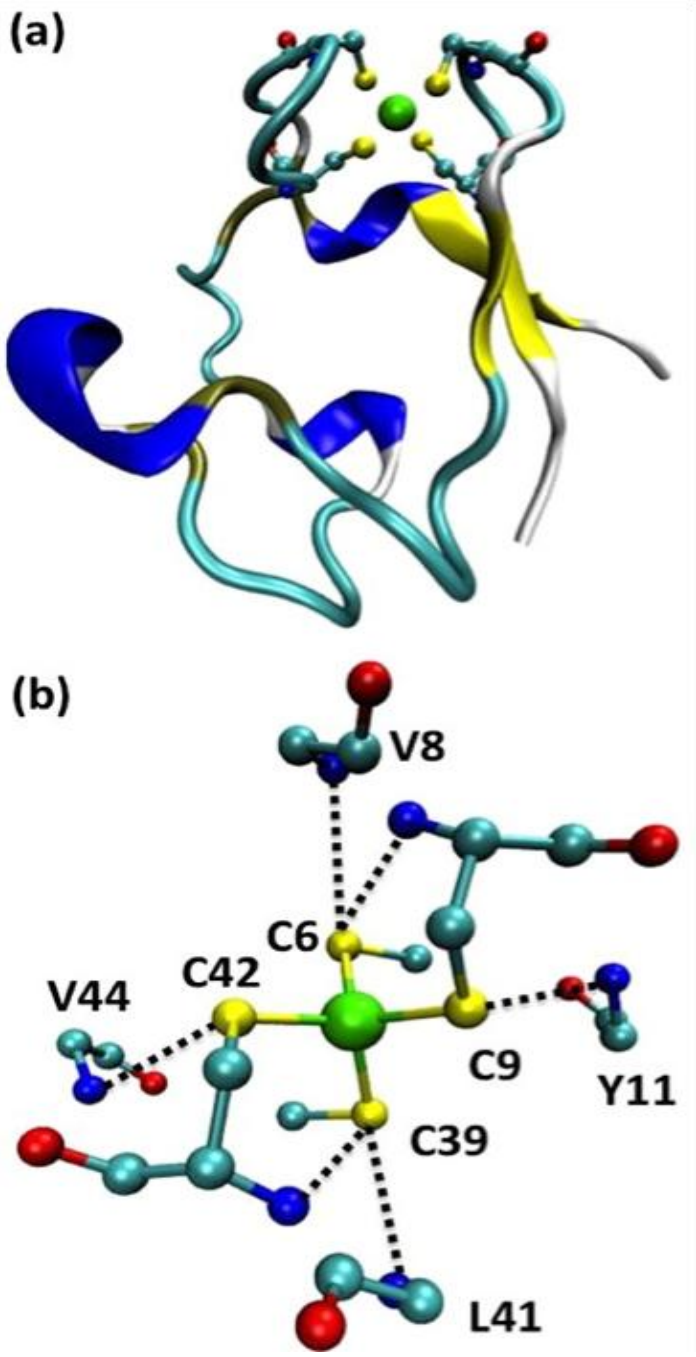

In its native environment, Rubredoxin from Pseudomonas oleovorans (PoRd) interacts with rubredoxin reductase to form an ET complex. PoRd facilitates the ET from rubredoxin reductase to a ω-hydroxylase bounding membrane, enabling the oxidation of aliphatic and aromatic hydrocarbons [14]. This ET process from NADH to Rd involves a rate-limiting adiabatic step [18,19]. Similarly, rubredoxin from Pseudomonas aeruginosa

(PaRd) contributes to alkane oxidation by shuttling electrons from NADPH, mediated by NADPH-rubredoxin reductase, to the final acceptor [22].

In anaerobic organisms, DgRd assumes a crucial role in the oxidative stress defense system [14]. It acts as a redox partner for NADH-rubredoxin oxidoreductase and rubredoxin-dioxygen oxidoreductase [14,23], participating in the transfer of electrons from ferredoxin-NADP+ oxidoreductase to superoxide reductase [14], thereby aiding in the reduction of O_2 or reactive oxygen species [24].

Moreover, Rubredoxin (Rd) exhibits associations with photosystem II (PSII) [14], which is proposed to either divert electrons from PSII to plastid membrane pathways or substitute certain electron transport proteins in photosynthesis [25,26]

Additionally, Rd demonstrates high electron self-exchange rates (kese) [14], indicative of its efficient electron transfer capacity. "For instance, the kese of CpRd" was determined to be $3\times105\ M^{-1}\ s^{-1}$ in 50 mM potassium phosphate, pH 7 at 30 °C" [14,25] [14,25].

Rubredoxins demonstrate reduction potentials near 0 Volts, displaying an approximate spread of 100 mV in both directions. The observed variation is affected by the interactions involving hydrogen bonding between the sulfurs of cysteine residues and adjacent amide protons [22,27]. This distinctive chemistry in Rubredoxin sparks significant interest in substituting metals, offering a cysteinyl potential coordination environment similar to other sulfur-rich contexts [26], such as cupredoxins [21,28], Cu-chaperones [23,29], zinc enzymes [30,31], bacterial [NiFe] hydrogenase [24,32], and molybdenum-containing proteins [33].

Rubredoxin derivatives serve as crucial tools for unraveling the structural and functional characteristics of metal sites containing sulfur-rich coordination spheres [26,34]. These metal-substituted Rubredoxins serve as valuable structural probes, shedding light on the intricate relationship between structure and function. Additionally, they act as bio-models, aiding in the modeling of intricate active sites found in native enzymes. Notably, the tetracysteinyl metal coordination site inherent in Rubredoxins exhibits versatility in accommodating a diverse range of metal ions. Up to this point, numerous metal-

substituted Rd variants have been synthesized and characterized [27], including those containing Fe(II) [30], Ni(II) [35,36], Co(II) [37], Cu(I) [38,39], Ga(III) [37], Zn(II) [40,41], Cd(II) [37], In(III) [42], Hg(II) [37], Ge(IV) [43], and Mo(VI, V, IV) [44].

1.3.1 Molybdenum-Substituted Rd: An Analog for Proteins Containing Molybdenum

Mo-Rubredoxin, with molybdenum substitution (Mo-Rd), was successfully synthesized from Desulfovibrio gigas (D. gigas) using an acidic dialysis method [28]. The primary objective of this process was to replicate the mononuclear molybdenum1 bis 1pyranopterin center found in "the DMSOR family" [34]. This involved coordinating of "the Mo atom with the four cysteine sulfurs and integrating exogenous ligands, including oxygen and sulfur atoms, thereby forming a Mo (VI)-$(S\text{-}Cys)_4$(=O) (X) complex (where X = –SR or-OH)" [34].

The confirmation of the molybdenum atom's presence within the tetracysteinyl metal binding site of rubredoxin was established through UV-vis spectral analysis. Notably, an absorption-band peaking at 278 nm (ε = 17.77 $mM^{-1}.cm^{-1}$) was observed, alongside two unresolved shoulders at 450 and 314 nm (ε = 1.02 and 8.01 $mM^{-1}.cm^{-1}$, respectively), attributed to molybdenum-thiolate charge-transfer bands [45].

Mo-S bending and stretching vibrational modes were provided by Raman spectroscopy, which suggests that the Mo-centre is involved in a coordination sphere of the Mo=O(–OH) type or Mo=O(=O…H–protein), which is comparable to the one found in the oxidized form of arsenite oxidase [46].

Electron paramagnetic resonance (EPR) demonstrated a stable $^{+}6$ oxidation state for the molybdenum center. This center exhibits reducibility, transitioning stepwise from $^{+}6$ to $^{+}4$ using sodium dithionite (E^0=-660 mV vs. NHE) as a strong reducing agent, involving an intermediate $^{+}5$ state. Intriguingly, weaker reducing agents like DTT (E^0=-3301 mV vs. NHE), while incapable of directly reducing the metal, can interact with it by binding as external thiol ligands [44].

Furthermore, the catalyst demonstrates remarkable biomimetic behavior, mimicking the key oxo transfer reactions of native mononuclear molybdenum enzymes. This is evidenced by its ability to promote the oxidation of arsenite ($As^{III}O_3^{3-}$) to arsenate ($As^{V}O_4^{3-}$), mirroring the behavior observed in native arsenite oxidase [47].

Scheme 1.2

Comparing the Coordination Geometry of Metal-Binding Sites in (a) Fe-Rd and (b)Mo-Rd [47]

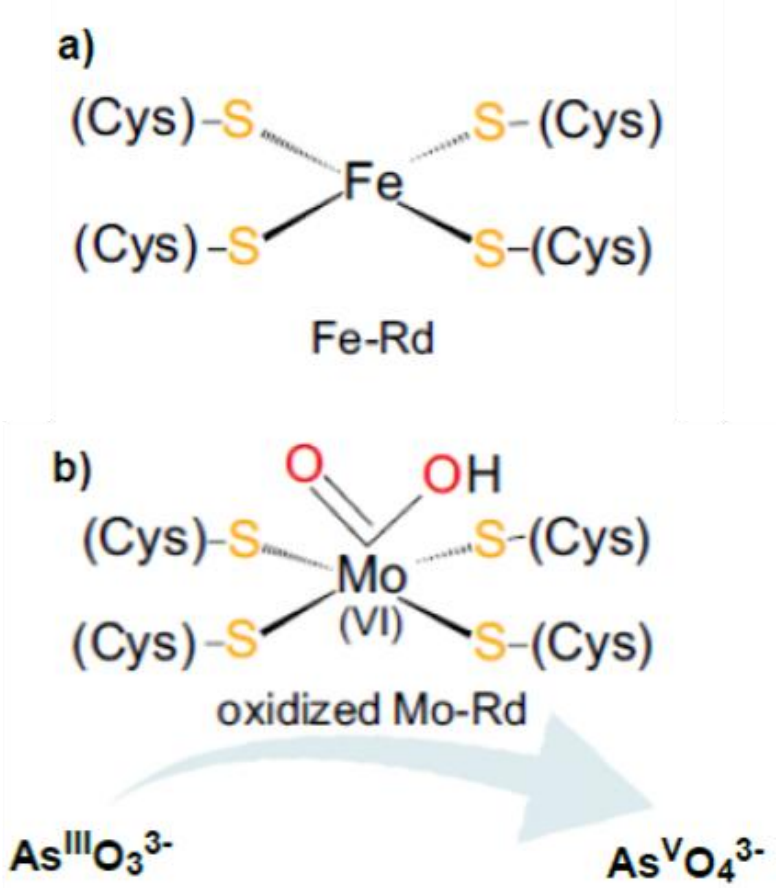

1.4 Molybdenum in Biology

Molybdenum (Mo) often overlooked as a crucial element for life, boasts a fascinating biological history stretching back nearly to Earth's origin. This transition metal possesses rich redox chemistry due to its electronic configuration: [Kr] $4d^5$ $5s^1$, enabling its access to a range of oxidation states (+2 to +6). However, under physiological conditions, Mo-oxidation states are predominantly +4 and +6. with notable exceptional states in some enzymes, such as the +3 state in the nitrogenases. This versatility empowers molybdenum-containing enzymes to play a vital role in various biological processes [48].

Despite being an essential trace metal found across all life domains, from archaea, and bacteria, to eukarya [36,37] Molybdenum exhibits a lower biological demand when compared to other essential metals like copper and iron [49]. Nevertheless, molybdenum remains a fundamental component as it serves as the foundation for several cofactors utilized by over 60 enzymes involved in the carbon, sulfur, and nitrogen biogeochemical cycles [39,40]. The versatility of molybdenum's primary coordination sphere contributes significantly to its involvement in biological processes, particularly enhanced by forming oxides and sulfides.

Moreover, molybdenum complexes exhibit a particular "atom exchanger" capability, especially in "oxygen atom transfer." This feature, combined with molybdenum's tendency to bind oxo groups and its ease in losing a single oxygen atom, has led many enzymes to harness its versatile chemistry to catalyze various atom-transfer reactions, including proton, sulfur, and oxygen atom insertions and abstractions, as well as both redox and non-redox hydration reactions [41,42].

The complex chemistry of the Mo atom requires careful regulation of its concentration inside cells to protect it from oxidative cellular environments and avoid redundant atom or electron transfer reactions [50] which is usually achieved through specific cofactors incorporated into apo-enzymes with dedicated proteins that end up creating fully functional metalloenzymes. In prokaryotes, molybdenum is transported within the cell by a high-affinity molybdate transporter. Under low-oxygen conditions, such as in sulfate-reducing bacteria, the molybdate anion inside the cell can convert to tetrathiomolybdate through oxygen-sulfur exchange processes [51–53].

1.4.1 Molybdenum Containing Proteins

Molybdo-proteins are proteins that contain a molybdenum (Mo) atom in their active sites. This group includes over 60 enzymes, which perform a variety of reactions due to the molybdenum atom's ability to switch between oxidation states (+4 to +6). This unique capability allows molybdoproteins to catalyze key reactions in the nitrogen, carbon, and sulfur biogeochemical cycles [49,54].

Molybdenum-containing proteins are classified based on how the molybdenum atom is coordinated with surrounding ligands. The first group includes proteins with a single Mo-atom bound to one or two pyranopterin cofactors at the active site. The second group consists of proteins with heteronuclear cofactors, such as those found in nitrogenase [55,56], the orange protein [57,58], and the molybdenum response protein [59]. Within the first group, Mo-dependent enzymes are further divided into three families: xanthine oxidase (XO), sulfite oxidase (SO), and dimethylsulfoxide reductase (DMSO) [49]. These families are distinguished by the number of pyranopterin cofactors and the type of additional ligands attached to the Mo center [25,50].

A single Mo atom binds with one or two pyranopterin cofactor molecules within these three mononuclear families. This interaction, mediated by "the cis-dithiolene (-S-C=C-S-) group", gives rise to the "molybdopterin (MPT) moiety" [26]. To further diversify functional capabilities, after the formation of the Mo-MPT (Moco) core, a second nucleotide can be appended to the structure. This attachment, typically involving cytosine or guanine, leads to the development of two additional variants: molybdopterin guanosine dinucleotide (MGD) and molybdopterin cytosine dinucleotide (MCD) [26]. This nucleotide diversification contributes to the functional repertoire of these enzymes, enabling them to participate in a wider range of metabolic processes [60].

The pterin cofactor plays a pivotal role in orchestrating both the structural organization of the metal, ensuring molybdenum's precise placement within the active site, and modulating the redox activity of the metal center [61]. Research indicates that the catalytic prowess is intricately tied to the specific 'environment' of the metal's first and second coordination spheres, significantly influenced by the pterin cofactor [26]. Acting as a conduit, this cofactor facilitates the transfer of electrons to and from the molybdenum atom, thereby enhancing intramolecular electron transfer processes [26]. Moreover, enzymes feature a binding pocket crucial for regulating the conformation of the pyranopterin cofactor, thereby selectively managing the structural isoforms of the pterin. This molecular regulation finely tunes the oxidation state of the metal, allowing for precise control over its chemical behavior and catalytic activity [52,53,62].

Furthermore, the reactivity of the metal is also impacted by additional atoms (oxygen, sulfur, and selenium) present in the metal coordination sphere [63]. Changes in the energy levels of the metal ground state d_{xy} orbital result in the modulation of the reduction potential of the Mo center [62,64]. The polypeptide chain imposes a specific ligand-coordination geometry, creating an "entatic state" that stabilizes and facilitates the association and/or dissociation of oxo- and sulfur groups. A comparison between a Mo atom coordinated with two pyranopterin cofactors (in a Mo-containing enzyme) and a synthetic model compound reveals distinctive geometric characteristics: the former adopts a trigonal prismatic coordination geometry, while the latter exhibits an octahedral geometry [65,66].

In these enzymes, a single Mo atom binds to one or two pyranopterin cofactor molecules, forming the molybdopterin moiety through the cis dithiolene group (-S-C=C-S-) [26]. To enhance functional diversity, a second nucleotide, usually cytosine or guanine, can be added to the Mo-MPT (Moco) core. This modification creates two additional variants: molybdopterin guanosine dinucleotide (MGD) and molybdopterin cytosine dinucleotide (MCD). These variants broaden the functional capabilities of these enzymes, enabling them to participate in a wider range of metabolic processes [60].

1.5 From Natural to Artificial Metalloproteins

Nearly half of all known proteins contain metal cofactors, which serve either structural or functional roles. Understanding how the protein environment influences the properties and reactivity of a metal ion is essential for uncovering the mechanisms behind key biological processes. This knowledge also allows researchers to design new metalloproteins with specific properties and novel reactivities. Much of our understanding of metal cofactor assembly and metalloprotein function has come from studies of natural metalloproteins and their mutants [67].

Despite significant advances, many questions remain unanswered. While the role of the primary coordination sphere in controlling functional specificity is well understood, the effects of medium- and long-range interactions are more complex. As a result, significant effort is being invested in developing metalloprotein mimics with the following goals:

Gaining deeper insights into the relationship between structure and activity, identifying the minimal structural requirements for functionality, replicating the functions of natural proteins in more compact, stable, and efficient systems, creating novel metalloproteins for applications in biomedicine, pharmaceuticals, and environmental contexts.

Designing metalloproteins is more challenging than designing conventional proteins because it requires not only a properly folded protein framework but also the precise inclusion of the correct number and type of ligands to match the coordination preferences of the metal center. However, most metal-binding sites have unique optical and magnetic properties, making them easier to characterize using spectroscopic techniques [1,68].

There are two main approaches to protein design: scaffold design and active site design [3]. Scaffold design involves constructing a polypeptide sequence that is unrelated to any natural protein (known as de novo design) [9]. Active site design involves modifying existing protein frameworks by introducing new metal-binding sites [3].

When choosing a design approach, using native protein scaffolds offers a broader range of options because of the vast number of protein structures available in the Protein Data Bank [1]. In contrast, de novo design offers greater freedom, as there is no theoretical limit to the number and types of structures that can be created from scratch.

Redesign strategies can be used either to introduce a new function or to change the metal specificity within natural metalloproteins [69]. Techniques like site directed mutagenesis have been widely used to explore the relationship between structure and function in metalloproteins. For example, when mutating highly conserved residues leads to a loss of activity, it helps identify the key residues responsible for a specific function. This knowledge can then be used to introduce new functions through the same mutagenesis approach.

Another design strategy involves miniaturization, which focuses on identifying the minimal peptide sequence necessary to replicate both the structural and functional aspects of a target metalloprotein's active site. Miniaturization can be systematically approached once detailed structural data for the natural system are available [70]. Key considerations

include: determining the type and number of components to assemble, defining the structure to be reconstructed, and specifying the function to be replicated.

1.6 Miniaturized Electron Transfer Protein (METP) Family

“Miniaturized proteins” are synthetic peptide based models inspired by natural macromolecular systems, designed to replicate specific structures and functions with the minimal necessary set of interactions [71]. Metalloproteins, with their central metal centers, are ideal candidates for miniaturization, as these centers serve as pivotal hubs around which varying sizes of coordination spheres form [72].

Electronic, redox and catalytic properties are established by the First Coordination Sphere (FCS) and are further modulated by the Second Coordination Sphere (SCS) and long-range electrostatic factors [13,73]. This miniaturization approach has been applied to rubredoxins (Rds), which are involved in electron transfer (ET) processes [73,74]. Rds from different species exhibit remarkable structural and metal-binding sequence similarities, characterized by two pairs of cysteine (Cys) residues arranged as “-Cys-$(X)_2$-Cys-(X)n-Cys-$(X)_2$-Cys”- [14,70,73,74].

The resulting miniaturized rubredoxin was named METP “Miniaturized Electron Transfer Protein”. Its coordination properties were explored with zinc and cobalt, in addition to iron, demonstrating METP's versatility in replicating the structures and properties of other proteins with tetrahedral metal-binding sites [47].

The METP design was based on the three-dimensional structure of DvRd, which served as a template. It was observed that a 17 Å sphere centered on the metal ion encompassed part of the molecule, including two type III β-hairpins [75]. These β-hairpins each contained “two Cys residues at positions i and i+3 within the type I-αRS α-turn” [76]. The backbone atoms of these structures exhibited approximate C_2 symmetry (Fig. S1).

Using C_2 symmetry simplifies design and reduces molecular size, making characterization easier. However, it also introduces the challenge of potential diastereomeric forms [77]. The METP model was conceived from a β-hairpin peptide with two appropriately spaced Cys residues capable of symmetrically dimerizing in the

presence of a tetrahedrally coordinating metal ion [70,78,79]. Initially, a pentapeptide sequence, Cys-$(X)_2$-Cys-X, was modeled in an α-turn conformation, with sulfur atoms oriented for tetrahedral metal ion binding. The resulting dimers were Λ and Δ enantiomers (Fig. S2 A and C), but due to the chirality of the amino acids, they were diastereomers. The configuration around the metal ion in Rd is Λ [80].

Efforts were made to address the issue of the two diastereomeric forms of METP. The two possible diastereomers were designed to contain inter-chain interactions that stabilize one isomer and destabilize the other [71,81]. Two pentapeptide sequences, Cys-$(X)_2$-Cys-X, adopting an α-turn conformation, were considered to provide the four Cys residues with the appropriate orientation for metal ion binding. However, these sequences proved too small to yield sufficient stabilizing or destabilizing inter-chain interactions [82].

1.7 From a Dimer to a Single Chain Mini Protein

A key strategy for achieving or improving the functions of designed metalloproteins involves introducing asymmetry. Following this approach, the minimal METP scaffold was engineered to introduce asymmetry around the metal center, resulting in a single-chain high-potential electron transfer mini protein named METPsc1 [83].

Despite spectroscopic characterization indicating that the METP prototype assumed the expected structural arrangement when coordinated with different metal ions [70,84], its iron complex was unable to perform reversible redox cycles. This was likely due to the low affinity of the tetrathiolate binding site for Fe(III), leading to the loss of the metal ion during redox cycling. Sacrificing symmetry to create monomeric analogs has been identified as a strategy to develop artificial iron-sulfur proteins capable of reversible redox cycling [83–85].

Scheme 1.3

Design and Structural Analysis of METPsc1

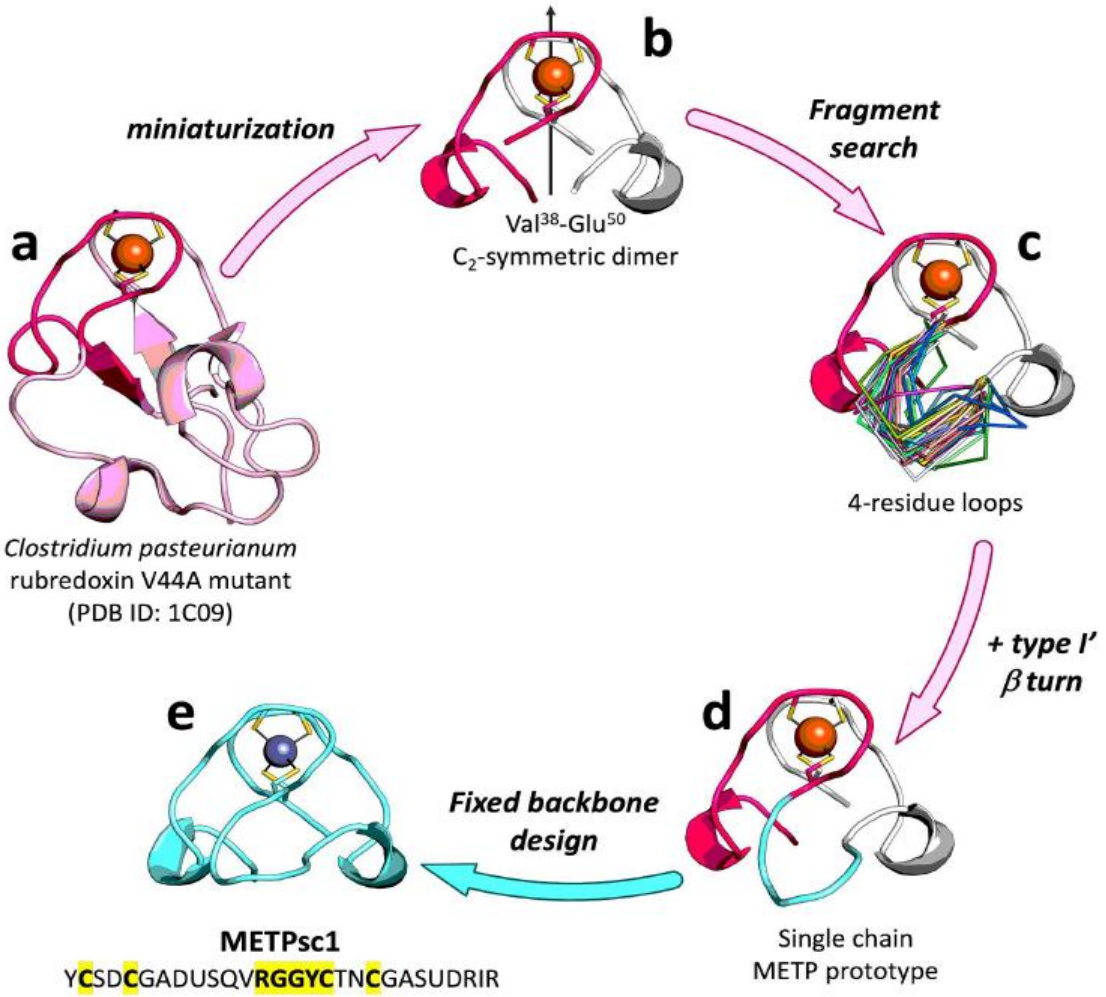

a)Crystal Structure of CpRd V44A Mutant. b) Miniaturized Model: Derived by implementing a C2 longitudinal rotation to the Val38-Glu50 segment of CpRd V44A. c) Overlay of 4-Residue Loops: Showcasing the various 4-residue loops identified during the fragment search. d) METPsc1 Prototype. e) Zn (II)-METPsc1 Model: Featuring the designed amino acid sequence, with "Cys and type I β-turn residues highlighted".[83]

1.7.1 Design of a Single-Chain Miniaturized Electron Transfer Protein

The development of the initial single-chain METP analogue (METPsc1) began with generating new backbone coordinates based on the high-resolution structure of the V44A mutant of CpRd in its reduced state. This mutant was chosen as the base model because of its higher redox potential compared to the native CpRd, a difference attributed to the V44A mutation (Scheme 1.3a) [86].

The segment from Val 35 to Glu 55 was extracted from CpRd, and a C_2 longitudinal axis was used to create the dimer coordinates (Scheme 1.3b) [83]. Following this, a systematic search was conducted to find the best fragment to connect the N-(Val 35) and C-(Glu 55) ends of the mirrored copy, with a maximum allowable gap length of seven residues.

The search involved plotting the number of fragments within 1 Å RMSD (Root Mean Square Deviation) of the backbone against the gap length. This analysis revealed that a four-residue loop was the shortest viable option for connecting the two ends, as shown in (Scheme 1.3c). Most of these loops contained simple β-turn motifs, with sequence analysis indicating that glycine residues predominantly occupied the i+1 and i+2 positions, a feature commonly seen in "type I'/III' β-turns" [87].

For the initial backbone model, we grafted the loop coordinates onto the previously established C_2-symmetrical dimer Val-Glu (Scheme 1.3d). A preliminary design routine was then performed to identify residue preferences at specific positions, and 2-amino isobutyric acid (AIB) residues were strategically placed at pseudo-symmetrical sites at positions 9 and 24 to promote the formation of a 310 helix [78].

Next, the identities of the X residues in the Cys-$(X)_2$-Cys motif were refined (Scheme 1.3e), focusing on restricting them to hydrophilic residues [83]. The final model was determined through further Monte Carlo sampling of the conformational space (300 runs), with the lowest energy structure selected (Scheme 1.3e).

The final amino acid sequence for METPsc1 is: "Ac-Tyr-Cys-Ser-Asp-Cys-Gly-Ala-Asp-Aib-Ser-Gln-Val-Arg-Gly-Gly-Tyr-Cys-Thr-Asn-Cys-Gly-Ala-Ser-Aib-Asp-Arg-Ile-Arg-NH_2". This design incorporates a combination of secondary and super secondary motifs [83], including a pseudo-C_2 axis of symmetry that relates two similar segments, each comprising: A short β-strand of 2 residues. An α-turn with Ser-Asp-Cys as corner residues [83]. A Gly β-bulge. Another short β-strand of 2 residues. An incipient 310 helix with two consecutive β-turns. Another short β-strand of 2 residues. A type I' β-turn featuring two consecutive Gly residues [83].

1.7.2 Zn(II)-METPsc1 Crystal Structure

X-ray diffraction analysis confirmed the zinc-complex structure of METPsc1, with Zn(II)-METPsc1 crystallizing within the orthorhombic space group $C222_1$.

All protein residues, including the N-acetyl and C-amide terminal protecting groups, were distinctly discernible within the electron density map and perfectly aligned with the intended protein sequence (Fig. S3 a) [83]. The overall backbone structure closely mirrored the designed structure (Fig. S3 b), along with the packing of Cys and hydrophobic sidechains. Surface-exposed sidechains exhibited alternative rotamers due to interactions related to packing and solvation. Notably, all the designed secondary and super-secondary motifs were evident in the experimental structure (Fig. S3 c) [83].

The peptide chain assumed a truncated cone shape, characterized by the following:

1. An upper base near the surface is formed by Cys20-Asp4 and Cys5-Asn19 residues, which constitute the metal binding site [83].
2. A lower base formed by the hydrophobic residues Aib9, Val12, Aib24, and Ile27, arranged to face each other, with their sidechains nearly aligned on a plane [83].

In addition, the two residues completing the coordination sphere, Cys2, and Cys17, occupied the inner space of the entire protein. In contrast, the remaining residues created a highly hydrophilic surface along the exterior of the conical structure [83].

A hydrated shell enveloped the macromolecule, and the crystal packing was reinforced by intermolecular salt bridges involving a residue of Arg26 and Asp4 from crystallographically related molecules. Furthermore, interactions between Tyr16 and its counterpart in a related METPsc1 molecule in the crystal lattice were also observed [83].

1.8 Aim of The Project

In this study, we focused on the Miniaturized Electron Transfer Protein single chain 1 (METPsc1) peptide, reconstituted to mimic a rubredoxin-like metal-binding site with a precise tetrathiolate environment. The reconstitution of the Molybdenum-Miniaturized Electron Transfer Protein single chain 1 (Mo-METPsc1) peptide was achieved using

varying peptide-to-metal ratios and was characterized through multiple spectroscopic techniques, including UV-Vis, Circular Dichroism (CD), and Magnetic Circular Dichroism (MCD) spectroscopy. Moreover, the spectrochemical investigation of its ET catalytic activities through exposure to catalytic activity to various reducing agents, sodium hydrosulfite (dithionite) and 1,4-dithiothreitol (DTT).

Chapter Two

Materials and Methods

2.1 Materials and Reagents

All starting materials and reagents, purchased from Sigma Aldrich and Merck, were of the highest available grade and used without further purification. The chemicals included Sodium molybdate dihydrate ($H_4MoNa_2O_6$; CAS Number 10102-40-6, purity of 99.97%), 2-mercaptoethanol (β-ME; $HOCH_2CH_2SH$; CAS Number 60-24-2), Milli-Q water, 2-Morpholinoethanesulfonic acid monohydrate (MES; $C_6H_{15}NO_5S$; CAS Number 145224-94-8) were purchased from Sigma Aldrich Co..

The prepared solvent systems: 0.1% (v:v) of Acetonitrile (ACN) with trifluoroacetic acid (THF), and 0.1% (v:v) of Water with trifluoroacetic acid, and Hydrochloric acid (100 mM) were purchased from Merck Co..

2.2 Equipments

- SephadexTM G-25 PD-10 desalting column (GE Healthcare).
- RP-HPLC (Shimadzu LC-10ADvp system equipped with an SPD-M10Avp).
- Inductively Coupled Plasma Mass Spectrometer ICP-MS (ELAN 9000, ICE 3xxx C113500021 v1.30).
- Cary 60 UV-vis spectrometer.
- JASCO J-1550 spectropolarimeter (JASCO, USA).
- stirrer plate
- pH Meter (STARA2110)

2.3 Molybdenum Reconstitution

The reconstitution process (Scheme 2.1) of the METPsc1 scaffold with molybdenum utilized Sodium molybdate dihydrate ($Na_2MoO_4 \cdot 2H_2O$) as the precursor compound, and 2-Mercaptoethanol (β-ME).

The reconstitution process began by mixing Na_2MoO_4 and beta-mercaptoethanol in a one-to-four ratio. This resulted in a dark orange solution displaying a prominent absorption

peak at 335 nm and a shoulder at 450 nm. These spectral characteristics are indicative of the formation of $MoO_2(SR)_4$ (where SR represents aliphatic thiol) [88–92]. Hence, within the reaction mixture, the probable complex formed is $\{MoO_2(\beta\text{-}ME)_4\}$.

An excess molar amount (1.5- to 2-fold) of the $\{MoO_2(\beta\text{-}ME)_4\}$ complex was introduced into an apo-METPsc1 solution dissolved in 200 mM MES Buffer at pH 6, and the mixture was incubated on an ice bath for 2 hours.

Scheme 2.1

Molybdenum Reconstitution Process Overview.

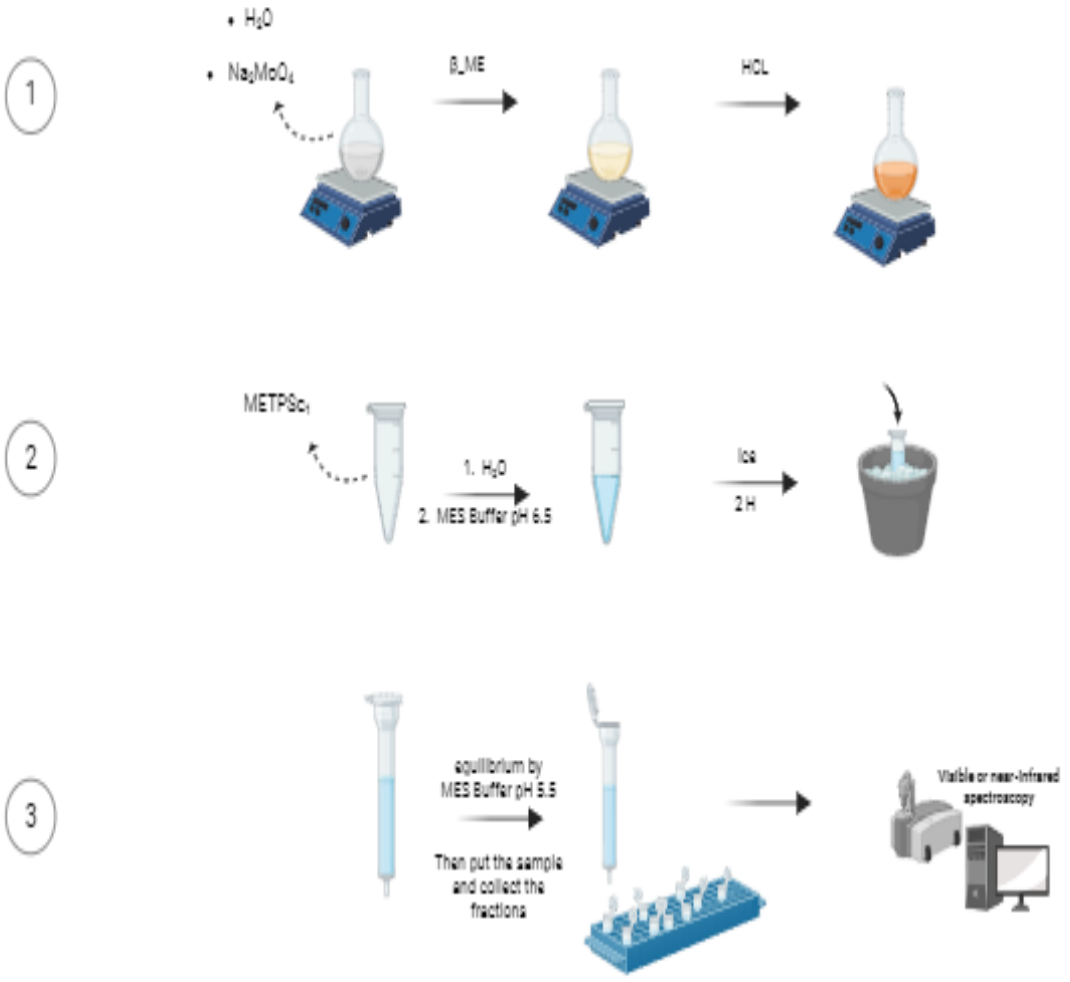

The initial stage involves $MoO_2(\beta\text{-}ME)_4$ complex formation, followed by protein reconstitution as the second step, and subsequently, collecting the fraction through PD-10 and examining the UV/Vis spectra as the third step.

To eliminate any residual-free metal complex {MoO2(β-ME)4}, the sample was passed through a "Sephadex TM G-25 PD-10" desalting column, which had been pre-equilibrated 25 mL of 50 mM MES buffer at pH 5.5. The Mo-METPsc1 elutes within the 3 mL of the equilibration [26,34,47].

Reconstitution attempts were avoided below pH 4 due to the instability and precipitation of apo-Rd under such conditions. Similarly, efforts were also refrained from above pH 6.5 because molybdenum within the $\{MoO_2(\beta\text{-}ME)_4\}$ complex showed reluctance in coordinating with protein cysteine thiols at higher pH values.

2.4 Metal Quantification: ICP-AES Analysis

Elemental analysis was conducted to determine the molybdenum concentration in the reconstituted Mo-METPsc1 peptide. An aqueous solution of 100 mL containing Mo-peptide was subjected to Inductively Coupled Plasma–Mass Spectrometry (ICP-MS). This analysis utilized a standard solution known as Reagecon 23, covering multiple elements within a concentration range of 0.05 to 3 ppm.

2.5 Spectroscopic Characterization

2.5.1 Absorption Spectroscopy

Ultraviolet-visible (UV-vis) spectroscopy was conducted using a Cary 60 UV-VIS spectrophotometer, and the resulting spectra were visualized using Cary WinUV for UV-vis Applications software. The measurements were carried out in 1 cm quartz cuvettes at room temperature and medium scan speed. The scanning interval was set at 0.5 nm, covering a spectral range from 250 to 800 nm.

2.5.2 Circular Dichroism (CD) Spectroscopy

CD characterization was conducted using a JASCO J-1550 spectropolarimeter that featured a temperature-controlled cell holder. CD spectra were gathered at a temperature of 20°C, spanning the range (600-260) nm with data intervals of 0.2 nm. The scan speed was set at 50 nm min^{-1}, utilizing a response time of 8 seconds and bandwidth of 2 nm. All measurements were performed using a 1 cm path-length quartz cell.

Analysis was conducted specifically on the tertiary structure fingerprint, encompassing disulfide bonds and aromatic amino acids, alongside investigations into ligand-Metal interactions (LMCT or metal d–d transitions), focusing exclusively on the Mo-METPsc1 form. These investigations were carried out by examining the near-UV region and the visible region (260 – 600) of the CD spectra. A 0.4 mM concentration of the Mo-peptide form was prepared within a 50 mM MES pH 5.5 buffer containing 0.5 mM TCEP for experimentation. The assessments were conducted using a quartz cuvette with a path length of 1cm, holding a total volume of 1400 µL.

Circular dichroism (CD) data can be presented in two main formats:

- Millidegrees (mdeg) of ellipticity (θ): This format displays the raw CD signal, measured in millidegrees, as it varies with wavelength. It's denoted as θ_λ (theta as a function of wavelength).
- Mean residue ellipticity ([θ]): This format adjusts for sample concentration, making it more standardized and comparable across different samples. It's calculated by correcting the raw CD data using (Equation 2.1).

$$[\theta]\left(deg.\frac{cm^2}{dmol}\right) = \frac{\theta_{obs}}{(10 \cdot l \cdot C \cdot n)} \ldots\ldots\ldots\ldots\ldots\ldots \text{Eq.2.1}$$

Where L is cell path length in cm, C is the protein molar concentration and n corresponds to the protein couplings numbers, which is in our protein equal to 29.

2.6 Reducing Test

Studies involving incubation were conducted to investigate the potential oxidation states of molybdenum within the Mo-METPsc1 scaffold. The assessment aimed to determine the reduction of the Mo atom, specifically from Mo^{6+} to Mo^{5+}/Mo^{4+}, through exposure to various reducing agents: sodium hydrosulfite (dithionite) and 1,4-dithiothreitol (DTT).

The experimental procedure commenced by adding one fraction of the Mo-METPsc1 peptide to a 1 cm quartz cuvette. Subsequently, 1 µL of dithionite (0.2 equivalents) was added. 2 µL of DTT (0.4 equivalents) was introduced along with another fraction of the peptide into a separate 1 cm quartz cuvette. After each addition, the solution was left to

incubate for 10 minutes with continuous stirring. The dithionite test was carried out anaerobically by degassing the solution with Argon, whereas the DTT test was conducted under aerobic conditions.

The spectral data were recorded using a Cary 60 UV/Vis spectrophotometer and visualized using the Cary WinUV for UV-Vis Applications software.

Chapter Three

Results and Discussion

3.1 Solid Phase Peptide Synthesis (SPPS)

The 28-amino acid sequence of METPsc1 was synthesized through automated solid-phase synthesis using an ABI 433A peptide synthesizer on a 0.25 mmol scale, following standard Fmoc chemistry. The synthesis employed an acid-labile H-Rink amide ChemMatrix resin with a substitution level of 0.45 mmol/g as the solid support (Figure 3.1) [93].

Figure 3.1

H-Rink amide ChemMatrix resin in Solid-Phase Peptide Synthesis (SPPS)

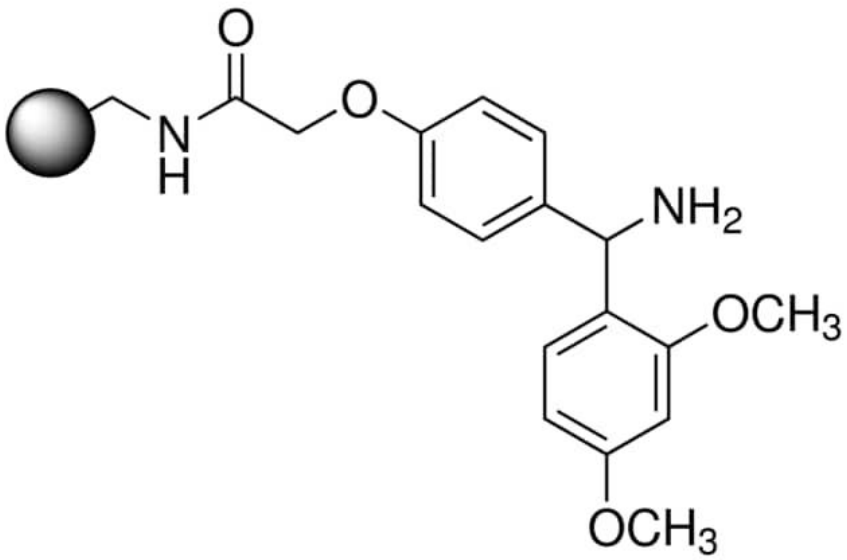

To activate the amino acids for coupling, we employed 2-(7-Aza-1H-benzotriazole-1-yl)-1,1,3,3-tetramethyluronium hexafluorophosphate (HATU) as the coupling reagent in situ. The N-terminal amino group was acetylated using a solution containing acetic anhydride, 1-hydroxybenzotriazole (HOBt), and diisopropylethylamine (DIEA) in N-methyl-pyrrolidone (NMP).

In most cases, a single coupling step sufficed for amino acid incorporation. However, for certain amino acids with hindered lateral chains, a double coupling was necessary due to less favorable coupling reactions. The progress of each coupling step was monitored by

assessing the yield via the conductivity of the solutions, relying on the formation of the Fmoc-piperidine salt.

Peptide cleavage from the resin and deprotection of sidechains were accomplished by treating the peptide with a mixture containing trifluoroacetic acid/H_2O/ triisopropylsilane/ethanedithiol at a ratio of 9.4:0.25:0.25:0.1 (vol/vol/vol/vol), resulting in an amidated C-terminus.

We included EDT in the mixture to prevent spontaneous oxidative reactions leading to disulfide bridge formation. H_2O was used as a proton donor, and TIS neutralized carbocationic species generated during the deprotection step.

The cleavage process was carried out with magnetic stirring for one hour in an ice bath and an additional hour at room temperature. Following cleavage, the crude peptide was precipitated in cold methyl tert-butyl ether and dried under reduced pressure. The yield of the crude peptide was determined to be 67% based on the resin substitution.

3.2 Identification and Purification

The crude METPsc1 underwent analysis by RP-HPLC, utilizing a Vydac C18 column (100 mm x 2.1 mm, 1.7 μm). The HPLC chromatogram of the METPsc1 exhibited a prominent peak emerging at 11.90 minutes, corresponding to the target product (Fig 3.2).

The product's identity was confirmed through mass spectrometry analysis. LC-MS chromatograms were generated using a Vydac C18 column (150 mm x 4.6 mm, 5 μm). In the mass spectrum, two prominent peaks were observed at 1485.45 m/z, representing the $[METPsc1 + 2H^+]^{2+}$ species, and at 990.85 m/z, corresponding to the $[METPsc1 + 3H^+]^{3+}$ species (Fig. 3.3 b). The anticipated monoisotopic mass was calculated as 2967.2 a.m.u. The experimental determination yielded a mass of 2968.8 a.m.u.

The initial purification of the crude METPsc1 was accomplished through reversed phase-flash chromatography, employing a Biotage SNAP C18 60g column. Subsequently, a second purification step was performed via preparative RP-HPLC, using a C18 column (250 mm x 22 mm, 10 μm).

To evaluate product purity, analytical HPLC was employed (Fig. 3.3 a), revealing a purity of 97.5%. The isolated peptide yielded an 18% recovery compared to the crude product. The pristine fractions were combined, subjected to lyophilization, and then stored at -20 °C.

Figure 3.2

RP-HPLC for the crude METPsc1

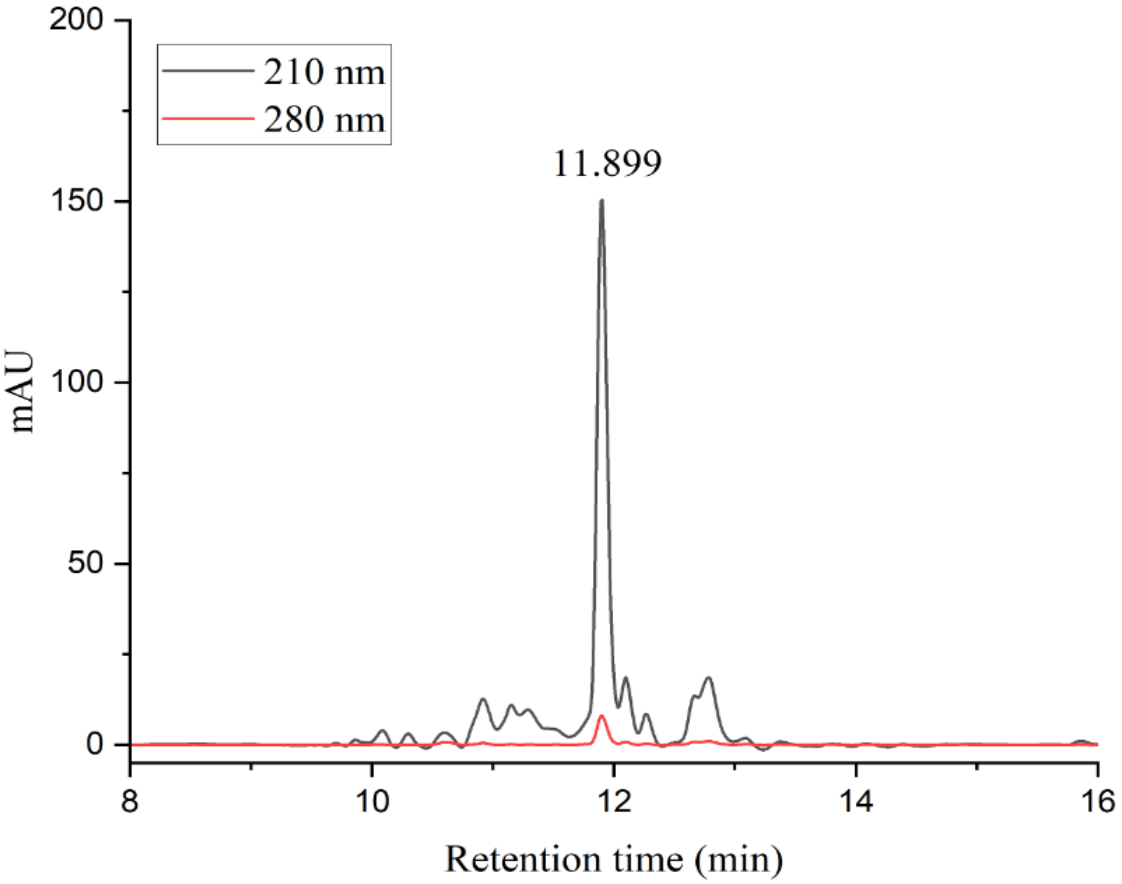

Figure 3.3

HPLC characterization (a) and the MS profile (b) of the METPsc1 pure fraction

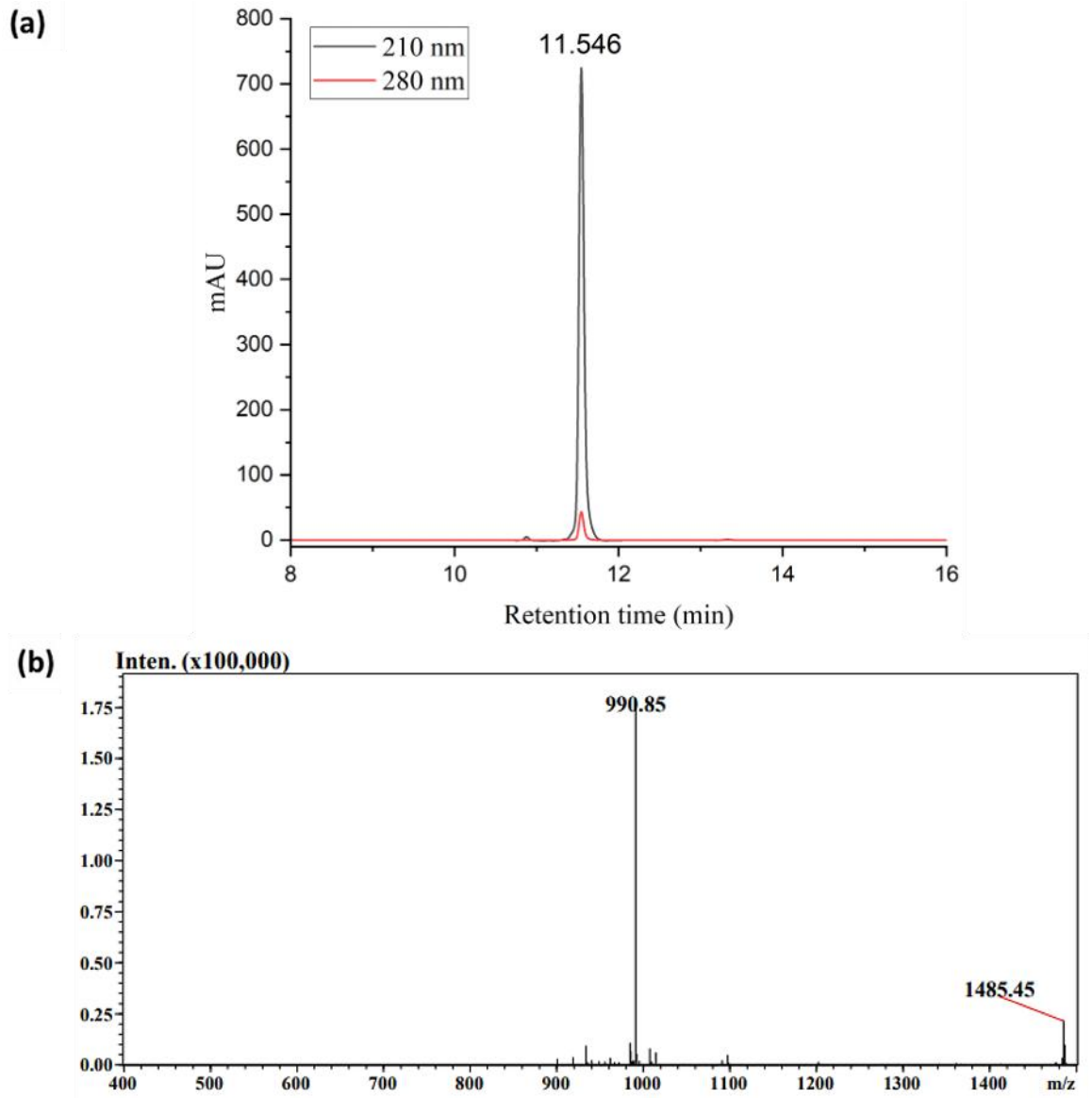

The pure fraction underwent RP-HPLC, with signal intensities measured at wavelengths of 210 nm and 280 nm. b) The mass spectrum corresponds to the primary peak identified in the crude METPsc1 sample.

3.3 Molybdenum Reconstitution and UV-Vis Characterization

The UV-vis absorption spectrum of Apo-METPsc1, a single-chain peptide, reveals an absorption band at 280 nm attributed to two aromatic tyrosine residues (Fig. 3.4). The molar absorption coefficient (ε) at 280 nm in H_2O at 273 K was determined to be 2980 M^{-1} cm^{-1} based on literature data [94]. This value was utilized for preparing all protein solutions at the desired concentrations.

The apo-METPsc1 peptide refolding was conducted under reducing conditions induced by TCEP to inhibit disulfide bond formation through cysteine residue oxidation and to improve the incorporation of metals. Following this, the peptide was incubated with various concentrations of sodium molybdate to β-mercaptoethanol, 1:4 and 1:4.7, maintaining fixed peptide-to-metal ratios of 1:2 Mo, and 1:2.5 Mo. The reconstitution procedure was carried out at 0 ℃.

In (Figure 3.5), UV-visible spectra obtained at room temperature under aerobic conditions illustrate the spectral changes resulting from the interaction of the Molybdenum atom with the tetracysteinyl environment within the metal binding site.

These findings indicate that elevating the concentration of molybdenum results in improved metal integration within the apo-METPsc1. The presence of two unresolved shoulders between 450-475 nm and 300-330 nm, representing thiolate-molybdenum charge transfer bands, resembling those observed in synthetic inorganic model complexes [92,95–100], confirms Mo incorporation. These transitions closely resemble those observed in the UV-Vis spectrum of the $(MoO_2(\beta\text{-ME})_4$ free compound, showcasing spectral maximum at 335 and shoulder at 450 nm.

Figure 3.4

UV-vis spectrum of apo-METPsc1(a), and Mo-METPsc1 (b)

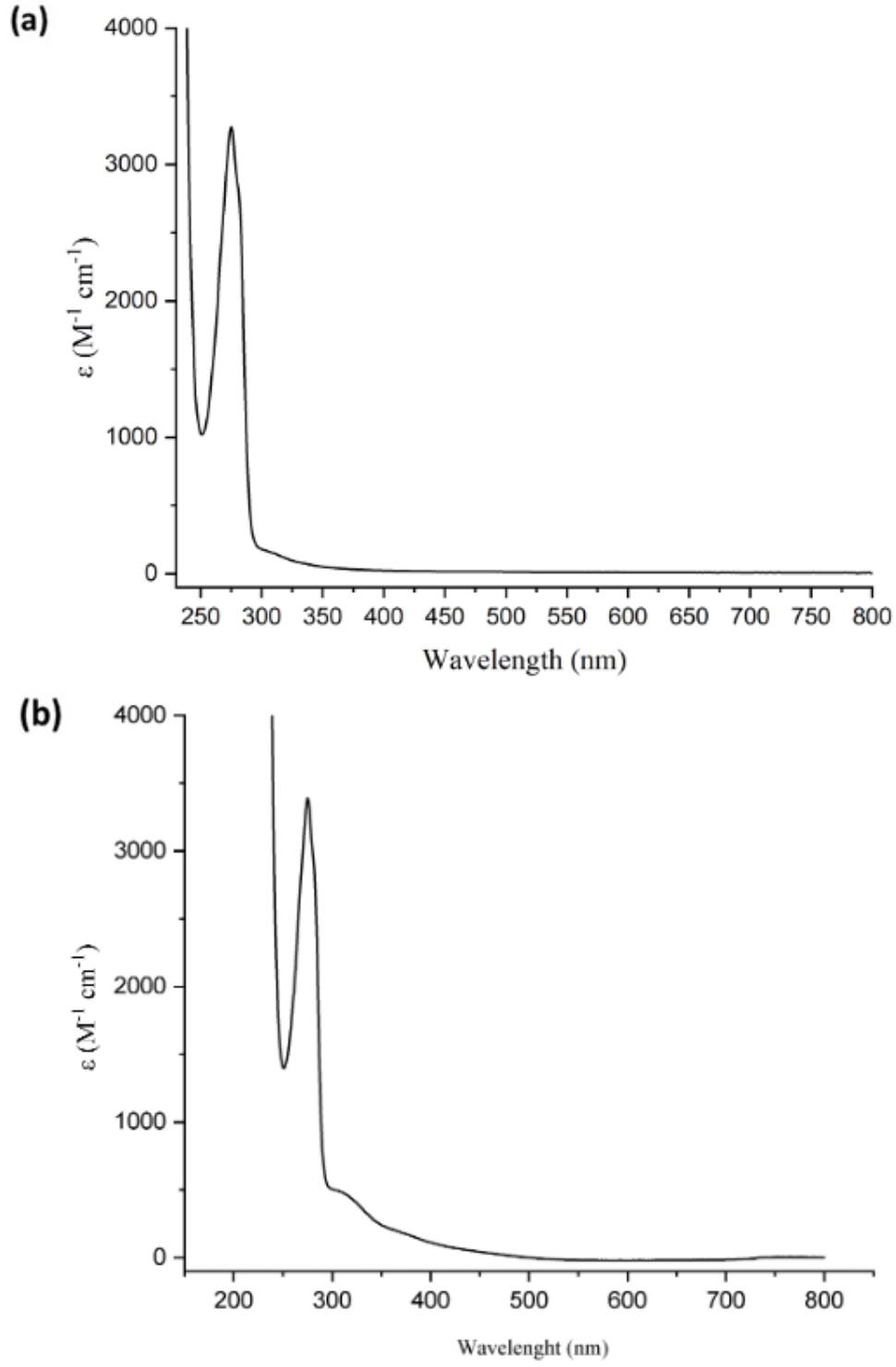

Figure 3.5

The UV-visible spectra of the peptide were examined for different metal ratios (a) and Variation in the $\lambda_{320}/\lambda_{280}$ ratio values concerning the diverse metal-to-protein ratios examined (b)

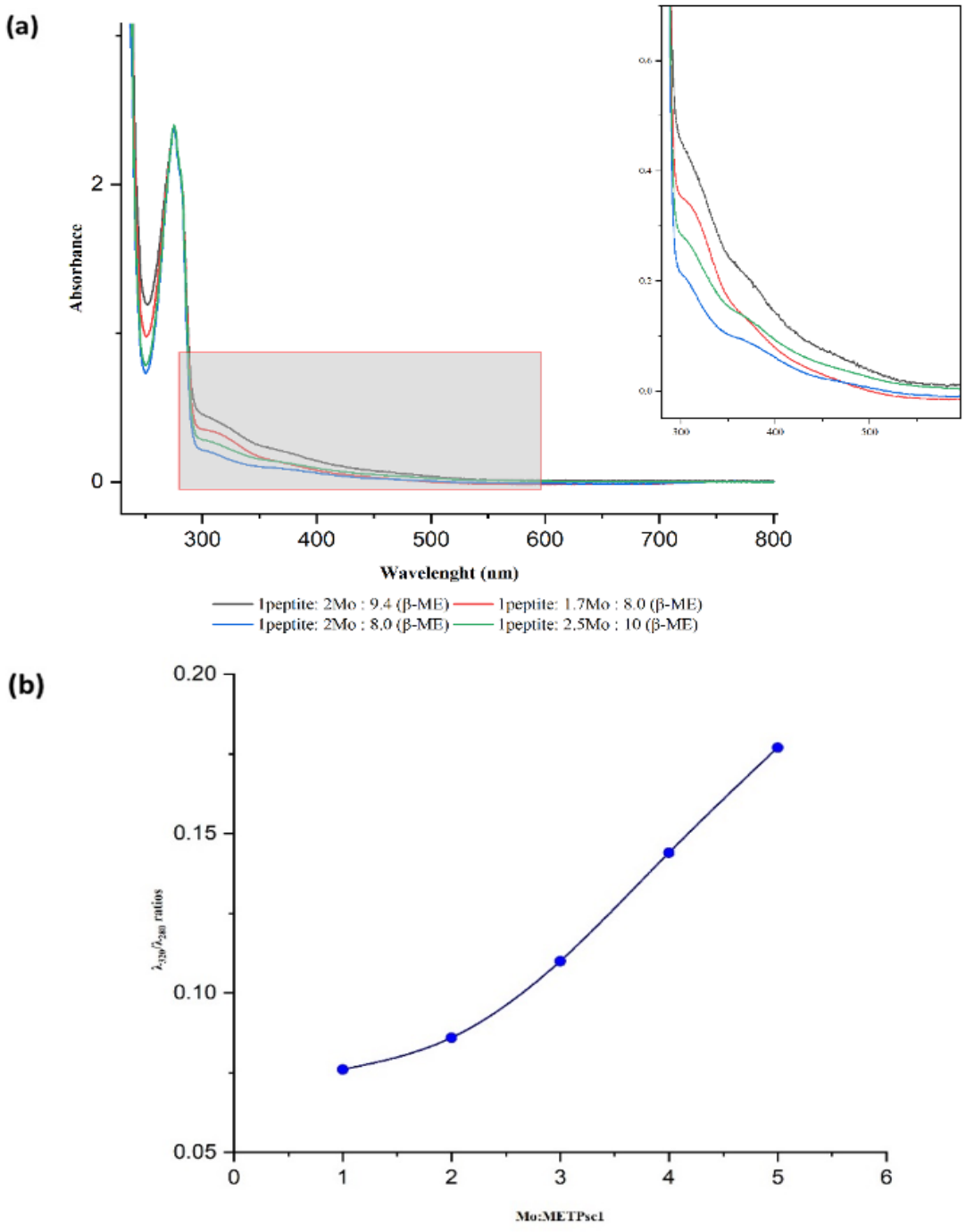

Each reconstitution process was carried out in a 50 mM MES buffer at pH 5.5 containing 0.5 mM TCEP (except the green one without TCEP). The experiment was conducted at room temperature. The spectra were normalized to account for variations in protein concentration.

The reconstituted Mo-METPsc1 exhibits a peak absorption maximum at 275 nm, alongside two unresolved shoulders at 320 and 470 nm. These spectral characteristics closely resemble those observed in Mo -substituted Rd redesigned by Maiti et al. In the Mo-Rd system, absorption peaks were observed at 278 nm, with two unresolved shoulders at 314 nm and 450 [101]. These findings were anticipated as both systems (Mo-Rd and Mo-METPsc1) feature the molybdenum atom coordinated within a comparable tetracysteinyl environment akin to a rubredoxin-like motif, thereby giving rise to Mo-thiolate charge-transfer bands.

Table 3.1 illustrates quantification data demonstrating a reconstitution efficiency of 4-6% at ratios of 1 peptide to 1.7/2 Mo atoms. This reconstitution is corroborated by UV-Vis spectral analysis, confirming the coordination of the metal within the specially engineered rubredoxin-like metal binding site.

Table 3.1

Incorporation Ratios at Different Reconstitution Ratios

Reconstitution ratio METPsc1: Mo	MoO_4: β-ME ratio	[Mo] by ICP Analysis (mg/L)	[Mo]/[peptide] Incorporation ratio	$\lambda_{320}/\lambda_{280\ ratio}$
1:2.5	1:4	1.7	0.04	0.112
1:7	1:4.7	3.3	0.06	0.144

Furthermore, upon observing the spectral development (Fig. 3.6), the addition of 1 micro of $\{MoO_2(\beta\text{-ME})_4\}$ complex resulted in a significant increase in absorbance ratio. This marked rise suggests a non-specific interaction between the metal and the peptide scaffold. Such non-specific interactions might stem from electrostatic interactions occurring on the peptide surface, rather than direct coordination with the cysteinyl sulfurs situated within the metal binding site.

Figure 3.6

UV-Vis monitoring of Mo-METPsc1

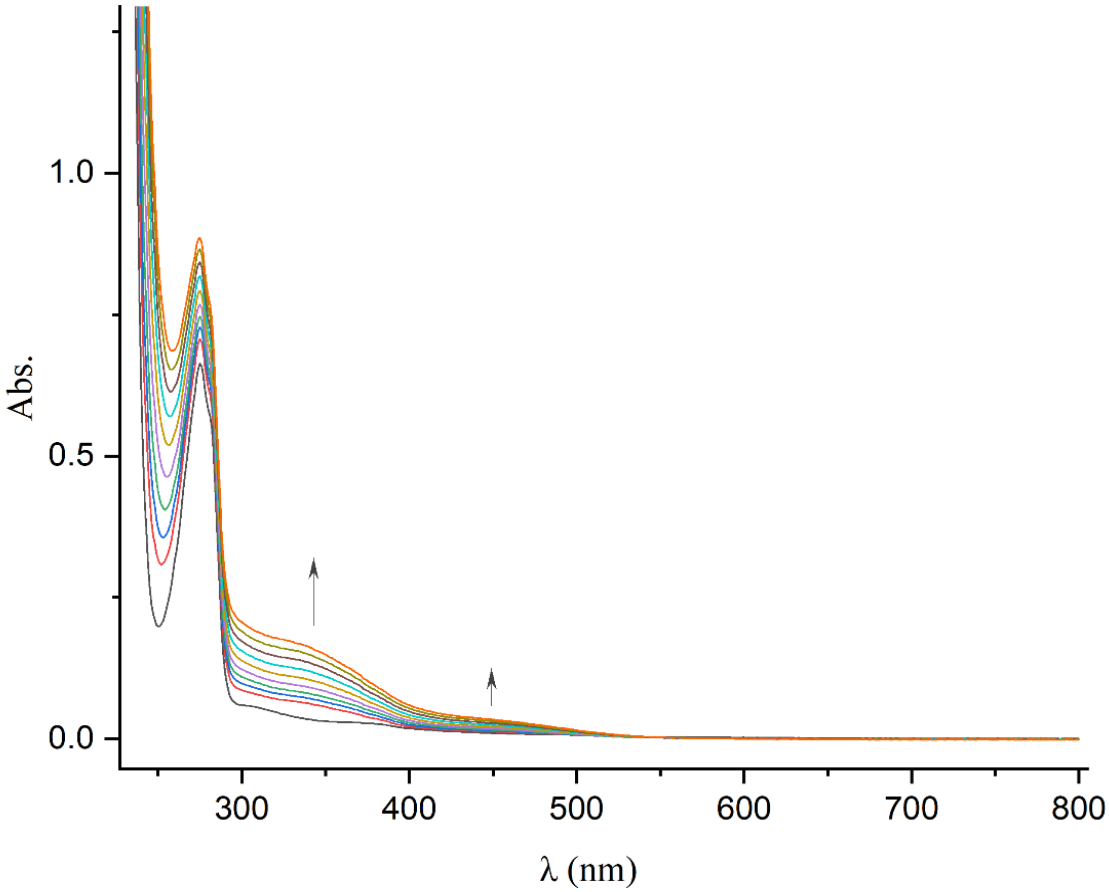

Notably, the selection of pH during the reconstitution process significantly influences the successful formation of Mo-Rd. As detailed in the "Chapter Two" section, pH levels ranging between 4.0 and 6.5 facilitate molybdenum incorporation and its coordination by the Rd cysteine thiol. A pH reduction to 5.0 was achieved by introducing drops of 100 mM Hydrochloric acid to the apo- MEPsc1-containing mixture alongside {MoO2(β-ME)$_4$}. A pH reduction to 5.5 can be achieved either by introducing acid to the apo-MEPsc1-containing mixture alongside {MoO_2(β-ME)$_4$}, or through dialysis against an acetate buffer at pH 5.5.

Nonetheless, in our study, the utilization of 100 mM HCL might influence the stability of the molybdenum complexes and the interaction between β-ME and molybdenum, potentially affecting the subsequent exchange with MEPsc1 cysteines during the

reconstitution process. On the contrary, in the dialysis to reach pH 5.5, successful reconstitution occurs. This is explained by the interaction of β-ME with molybdenum, which then gradually replaces MEPsc1 cysteine thiols during the dialysis process.

3.4 Circular Dichroism (CD) Characterization

3.4.1 Far-UV Absorption CD Characterization

CD emerges as an invaluable spectroscopic method for probing the secondary structures of peptides and proteins. It operates on the principle of dissimilar absorption between left- and right-handed circularly polarized light by a chromophore within an asymmetric environment. This chromophore primarily resides in the amide bond in peptides and proteins, displaying substantial absorption within the far-ultraviolet (UV) spectrum range, typically from 190 to 250 nanometers (nm).

The wavelengths and intensities of the CD signals detected within this spectral range are contingent upon the spatial orientation of peptide bonds, serving as indicators of the peptide's conformation. Remarkably, specific secondary structures like α-helices and β-sheets exhibit unique CD spectra. For instance, the α-helix manifests two negative minima, roughly at 222 nm (related to the amide transition n-π*) and 208 nm (related to the amide transition π-π*), alongside a positive maximum near 194 nm (related to the amide transition π-π*, indicating perpendicular coupling).

Conversely, the β-sheet CD spectrum showcases a negative band at around 215 nm (related to the amide transition n-π*), a distinctively strong positive peak near 198 nm, and another negative minimum around 175 nm (related to the amide transition π-π*). The random coil structure is also discernible through an intense negative band at approximately 197 nm resulting from the electronic transition π-π* and a weaker positive band at around 218 nm attributed to the electronic transition n-π* [102,103].

Moreover, CD spectroscopy proves instrumental in examining conformational alterations and stability changes after metal binding in native proteins and artificially designed peptides [81].

3.4.2 Near-UV and Visible Region CD Characterization

CD investigations within the near-UV region uniquely characterize the protein's tertiary structure. Within this spectral region, the observed contributions stem from transitions occurring within the surrounding environment of individual aromatic residue side chains, namely tyrosine, phenylalanine, and tryptophan. Additionally, there might be contributions stemming from disulfide bonds, yet their intensity in the transition is notably fainter compared to the contributions from aromatic amino acids. The primary sequence of the METPsc1 scaffold includes tyrosine (Tyr) residues, which are aromatic.

Figure 3.7 displays a near-UV/Vis spectral comparison between the apo- and Mo-METPsc1 peptides under TCEP-induced reducing conditions, wherein the aromatic amino acid contributions exhibit a heightened and more distinct appearance. This phenomenon could be attributed to alterations in the surrounding environment of individual side chain residues. These changes might involve electrostatic interactions, additional hydrogen bonding, and effects on polarizability induced by the reducing agent TCEP. Specifically, the contributions from tyrosine are observed within the wavelength range of 270 to 285 nm.

Nonetheless, the broader near-UV spectral profile observed in the apo-METPsc1 implies the possibility of additional spectral contributions, potentially stemming from the formation of disulfide bonds within the tetra cysteinyl environment. Despite the apo-scaffold spectrum being less sharp and defined compared to the Mo-counterpart, the overall similarity in peak profiles indicates some subtle changes in the tertiary structure upon metal-binding.

Circular dichroism investigations in the visible spectrum prove valuable for analyzing charge-transfer transitions occurring within metal-ligand complexes.

An example is the Mo-METPsc1 scaffold, housing a molybdenum atom within a tetra cysteinyl environment, leading to distinctive Mo-thiolate transitions. This coordination induces a chiral setting within the metal-binding site, generating a specific CD signal within the visible spectrum.

In the presence of TCEP, Circular dichroism data obtained from the Mo-METPsc1 scaffold displays a prominent absorption range at 350-500 nm (Fig. 3.7 b). This distinct spectral feature within the visible range, confirms the effective insertion of the Molybdenum atom within the rubredoxin-like metal binding site.

Figure 3.7

Circular Dichroism spectra of both apo- and Mo-METPsc1 peptides near UV (a). And Vis (b)

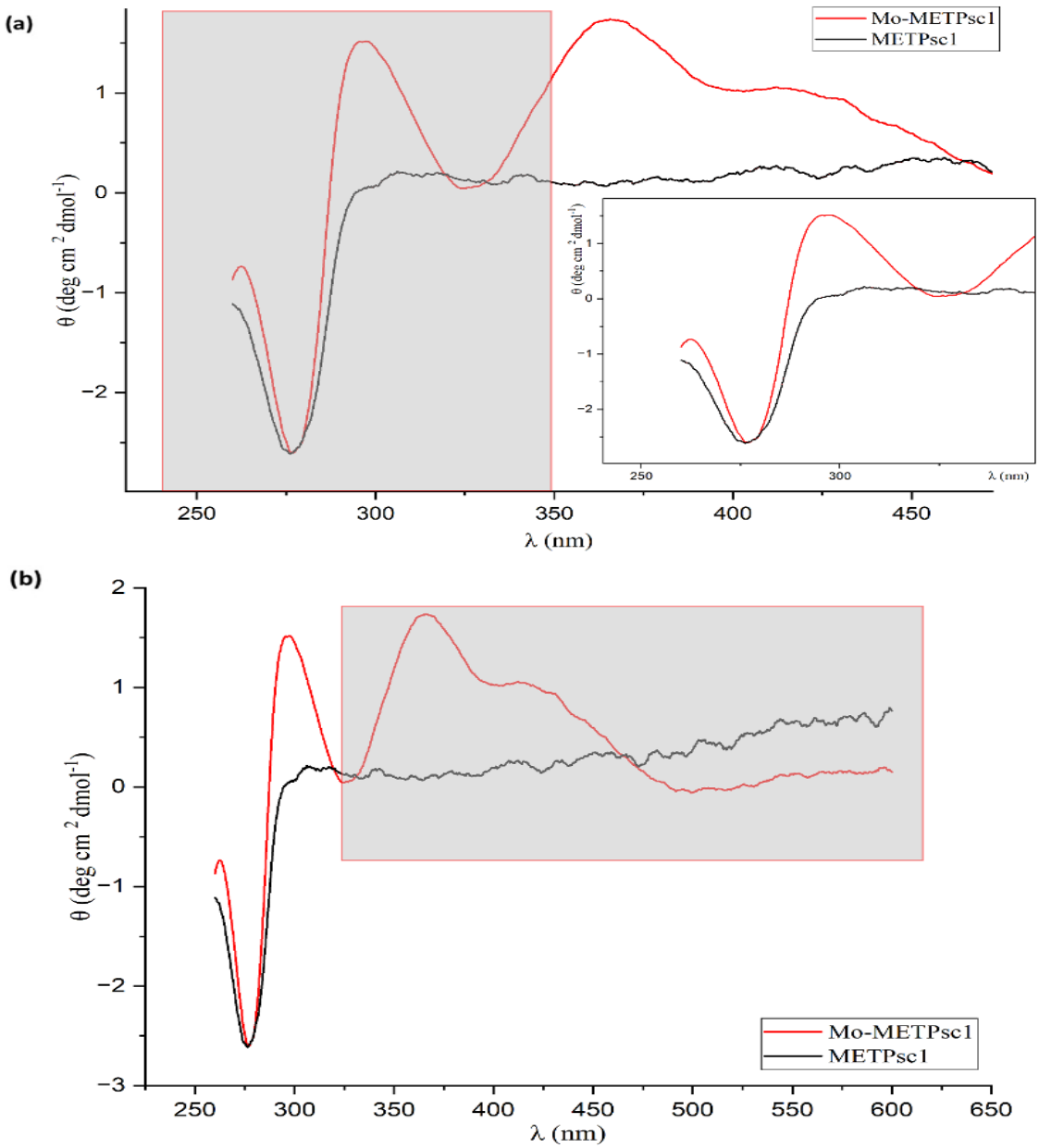

The peptide concentration was 0.4 mM under TCEP-reducing conditions in a 50 mM MES Buffer at pH 5.5. These spectra were obtained using a 1cm pathlength cuvette at 20°C.

3.6 Oxidation-state characterization: Reducing tests

In the investigation of metal oxidation states within the METPsc1 scaffold's tetracysteinyl environment coordinated with the Mo atom, incubation studies were conducted. Studies involved distinct incubations utilizing different reducing agents- sodium hydrosulfite (dithionite) in an anaerobic setting, and 1,4-dithiothreitol (DTT) in aerobic conditions. The tests employing 0.4 equivalents of DTT (Fig. 3.8) and 0.2 equivalents of dithionite (Fig. 3.9) yielded comparable outcomes, and induced changes in the UV-vis spectral profile of the Mo-peptide.

Figure 3.8

UV Visible Spectroscopic Analysis of the Incubation Experiment with DTT

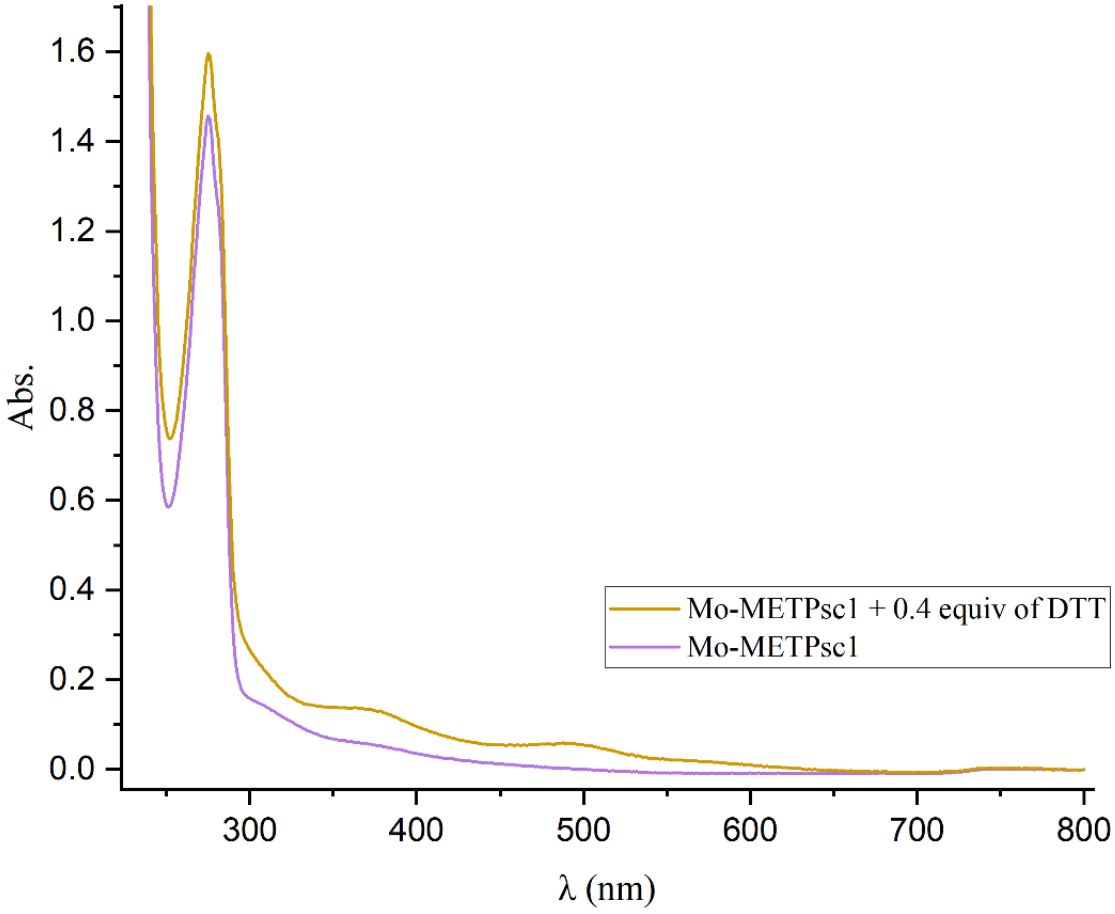

The incubation was conducted with 0.4 equivalents of DTT, under anaerobic conditions, within a 50 mM MES buffer, pH 5.5.

Figure 3.9

UV Visible Spectroscopic Analysis of the Incubation Experiment with Dithionite

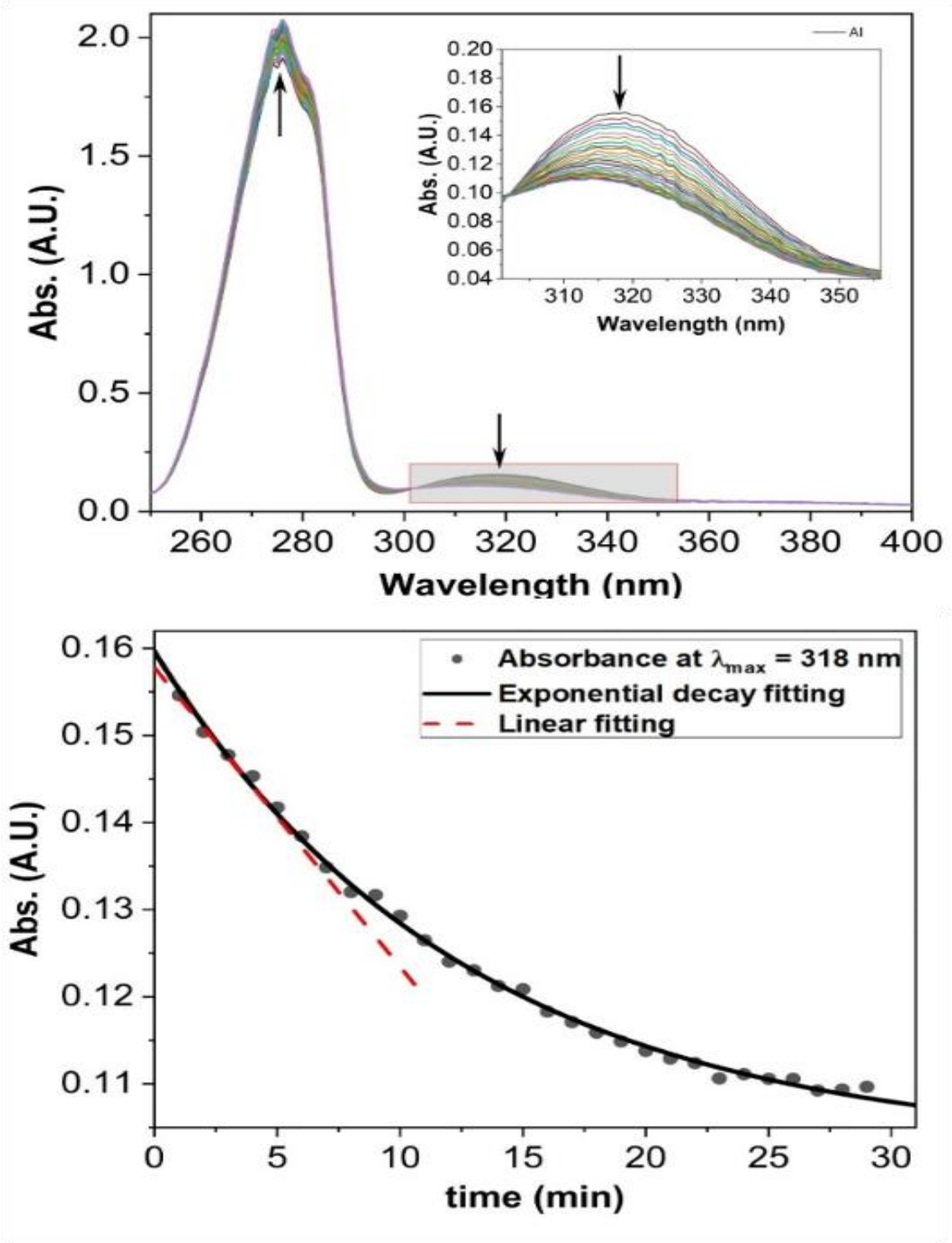

The incubation was conducted with 0.2 equivalents of sodium dithionite, under anaerobic conditions, within a 50 mM MES buffer, pH 5.5.

An elevation in absorbance within the Molybdenum-thiolate charge-transfer spectral range (300 – 400 nm) indicates a heightened involvement of charge transfer transitions. This rise could stem from either the metal reduction, transitioning from Mo^{6+} to Mo^{5+}, or from the metal forming additional coordination with a sulfur atom from an external thiol compound. A comparable response was observed in the DTT-treated Mo-Rd derivative. Here, the emergence of a UV-Vis band at 336 nm and 460 nm potentially indicates the incorporation of sulfur by an external thiol ligand into the Mo center [101].

Figure 3.9 shows a one-phase exponential decay function, which is commonly used to describe first-order kinetic processes.

The R-squared value (0.997) for the exponential decay model is very high, which suggests that this model fits the data well. The R-squared value (0.983) for the linear regression model is also quite high, which may indicate that the relationship between absorbance and concentration in this system is approximately linear over the time range shown.

The data estimation indicates DTT's inability to reduce the Mo atom (in the next section). Conversely, dithionite exhibits a notably higher efficacy in reducing the Mo center than DTT. This deduction finds further substantiation from the consistent UV-Vis spectra of the Mo-METPsc1 treatment with 0.4 to 1.2 equivalents of DTT. In contrast, the intensity of the Mo-thiolate charge-transfer region in the spectra of the dithionite-treated Mo-peptide decreases with increasing dithionite concentration beyond 0.2 equivalents.

3.5 Magnetic Circular Dichroism (MCD) Characterization

Magnetic Circular Dichroism (MCD) spectroscopy serves as a potent tool for delving into the electronic framework and transitions within paramagnetic sites present in molecules or metalloproteins. Specifically focusing on molybdenum organized by four cysteine residues in a tetrahedral configuration, MCD analysis yields valuable insights into the electronic transitions occurring at the molybdenum center.

Figure 3.10

MCD spectra of Mo-METPsc1 peptide (a). And Mo-METPsc1 with DTT (b)

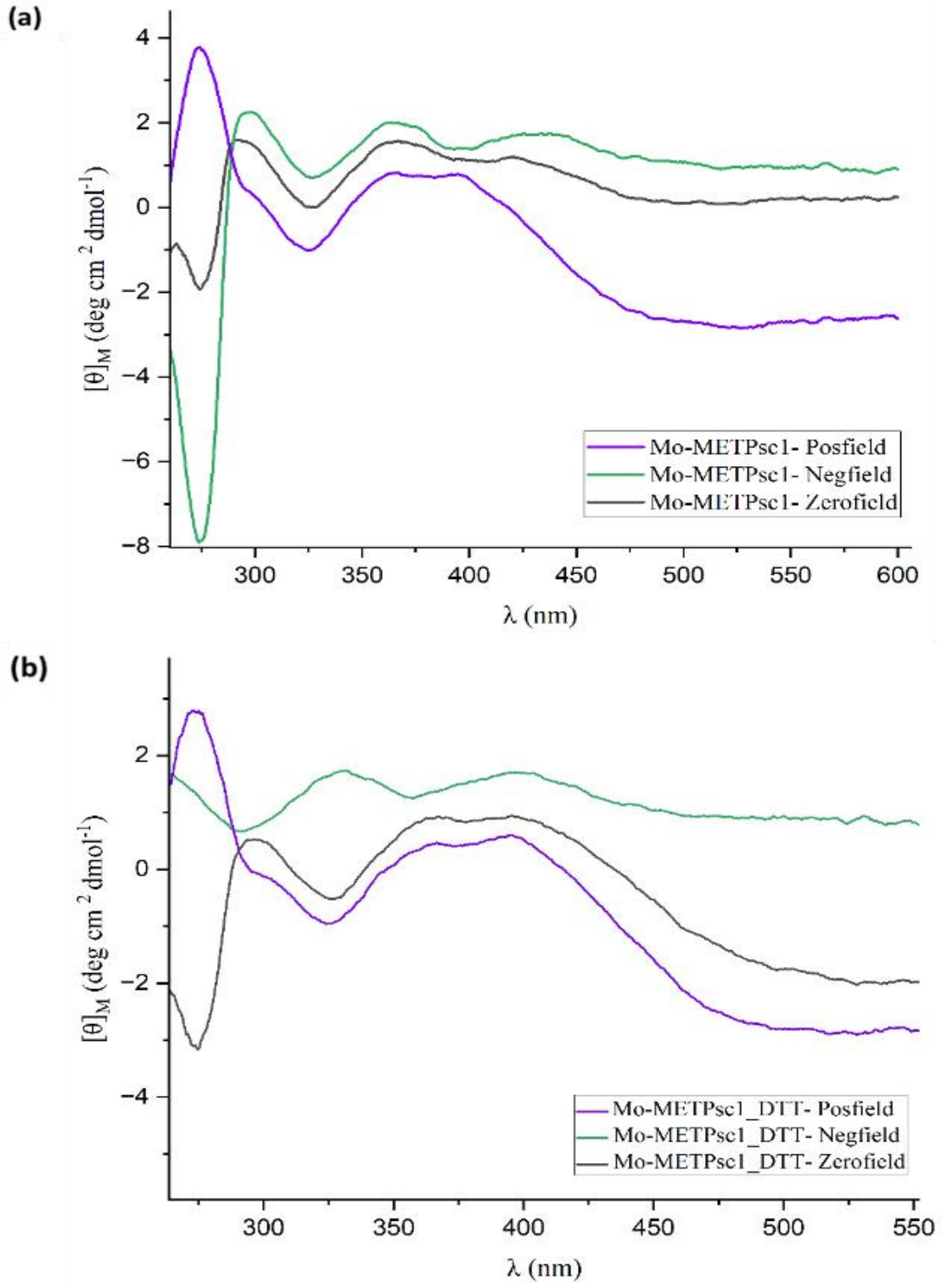

The peptide concentration was 0.4 mM under TCEP-reducing conditions in a 50 mM MES Buffer at pH 5.5. These spectra were obtained using a 1cm pathlength cuvette and for b) the magnetic field 0.9 Tesla.

In the near-UV spectrum, MCD signals likely stem from charge transfer transitions between the cysteine sulfur atoms and the molybdenum center, shedding light on the nature of these transitions. These specific transitions elucidate the intricate electronic interactions between the cysteine ligands and the molybdenum ion, contributing significantly to the resultant MCD spectrum.

Moving into the visible region, MCD peaks probably signify transitions involving the d-orbitals of the molybdenum center. These transitions might encompass ligand-field transitions or other distinctive electronic interactions characteristic of the tetrahedrally coordinated molybdenum-sulfur environment.

The MCD spectrum obtained from such a molybdenum complex would provide information about the nature and energies of electronic transitions, the coordination geometry, and the ligand-field interactions.

While the CD spectrum showcases robust extrema, both positive and negative, in the near UV/visible range, the Mo-METPsc1 displays weak positive extrema at 375 and 395 nm, 430 nm alongside a negative extremum at 325 nm and 274. In the corresponding MCD spectrum (Figure 3.9 A) a negative Faraday effect is observable alongside a positive Faraday effect.

MCD spectroscopy served as a tool to explore the electronic structure of Mo-METPsc1. A band observed at 500 nm (22,250 cm^{-1}) linked to an $S_{\sigma(cysteine)} \rightarrow Mo_{(xy)}$ Ligand Metal CT transition. This spectral assignment led to the inference that the cysteine groups in coordination reduce the effective nuclear charge of the Mo ion and shift its reduction potential to more negative values through S→Mo charge donation. Higher-energy MCD features appeared at 374 (26,500 cm^{-1}) and 325 nm (31,000 cm^{-1}), tentatively attributed to a $S_{cys} \rightarrow Mo_{(xy)}$ LMCT transition.

Furthermore, in assessing the oxidation state of molybdenum, the MCD spectra demonstrate a peak profile akin to that observed in CD, exhibiting no shift in wavelength or energy.

The MCD spectra of the Mo-METPsc1 peptide under DTT-induced reducing conditions were also examined (Fig. 3.10 b). Upon aligning this data with the subsequent section's analysis on reducing studies, this indicates an inability of DTT to reduce the Mo-center while suggesting the potential efficacy of dithionite for achieving such reduction.

Nevertheless, the Mo-METPsc1 peptide treated with DTT implies potential coordination involving the sulfur atom of this external thiol ligand with the Mo-center, similar to the observation noted in the DTT-treated Mo-Rd derivative.

Chapter Four

Conclusion

4.1 Conclusion

In conclusion, the study successfully reconstituted Rd with molybdenum, suggesting the presence of a Mo=O(OH)(–SCys)$_4$ center or a Mo=O(SR)(–SCys)$_4$ center.

The incorporation of metal in the tetracysteinyl active site was determined by observing two broad absorption bands. These bands, characteristic of thiolate-molybdenum charge transfer, emerged at 320 nm, and 450 nm.

Additionally, Visible CD spectroscopy further strengthens the evidence for a strong peptide-metal interaction. This is indicated by the emergence of a broad, positive absorption band peaking at 350-500 nm, which is not observed in the CD spectra of either the apo-peptide or the MoO_2(β-ME)$_4$ compound.

Interestingly, upon reduction with DTT and dithionite, the UV-vis spectrum shows an increase in the thiolate-molybdenum charge transfer region. This might suggest further coordination of the Mo-atom with an external thiol ligand, similar to observations in the molybdenum-substituted derivative of rubredoxin.

4.2 Future Perspectives

In the future, we plan to conduct additional spectroscopic characterizations and activity studies to confirm the newly designed Mo-METPsc1 peptide. These spectroscopic investigations will encompass two critical techniques: Raman spectroscopy and EPR spectroscopy. These techniques are indispensable for verifying the oxidation state of molybdenum, define the redox process within the tetra cysteinyl environment, and establish the first coordination sphere in the reconstituted Mo-METPsc1 and the thiol-treated Mo-METPsc1.

Resonance Raman investigations will provide insights into the composition of the first coordination sphere. This will be determined by observing the presence of broad cysteinyl S-Mo^{5+} charge transfer bands, typically around ~400 nm, and by analyzing the Mo-S

bending and stretching vibrational modes, which typically occur between 300 - 400 cm^{-1}. Moreover, the potential expansion of the Mo coordination sphere involving hydroxyl groups or oxygen atoms can be examined.

19F-NMR spectroscopy studies can be employed for the conclusive assessment and supplementation of the expanded Mo coordination number. This method verifies the binding of an exogenous thiol ligand within the active site, consequently forming a $Mo{=}O(SR)(–SCys)_4$ center.

EPR (Electron Paramagnetic Resonance) proves to be an appropriate technique for tracking the reduction process of the oxidized Mo-METPsc1 scaffold using dithionite or DTT. This involves observing the transition from Mo^{6+} to Mo^{5+}. Moreover, extending the duration of the reduction process can provide insights into whether the Molybdenum-tetra cysteinyl center is capable of undergoing a two-electron transfer reaction. By monitoring the reduction time, it becomes possible to observe the changes in signals and infer the progression of the reaction involving the Mo-tetracysteinyl center.

CV (Cyclic Voltammetry) spectroscopy, alongside supplementary electrochemical assays, will serve as valuable complements to the EPR studies. These techniques will provide additional insights and data regarding the redox behavior and electrochemical properties of the Mo-α3DIV-L21C scaffold.

Furthermore, it's crucial to conduct studies examining the pH-dependent behavior of the Mo-METPsc1. Understanding how the scaffold's properties and reactivity change with variations in pH levels is essential for a comprehensive understanding of its functionality.

Moreover, investigating the binding affinity between molybdenum and the peptide is equally important, if feasible. Determining the strength and nature of this interaction sheds light on the stability and specificity of the Mo-peptide complex, contributing significantly to understanding their relationship and potential applications.

Once we conclude the structural characterization studies, we will examine the catalytic capabilities of the metal active site. The specific activity studies will be tailored to the metal's first coordination sphere. We can test its ability to oxidize arsenite to arsenate or reduce dimethyl sulfoxide to dimethyl sulfide, modeling enzymes like (A. faecalis) and (R. sphaeroides), respectively.

List of abbreviations

Abbreviation	Meaning
D. gigas	Desufovibrio gigas
Rd	Rubredoxin
DMSOR	Dimethylsulfoxide Reductase family
DMF	N, N-dimethylformamide
DTT	Dithiothreitol
β-ME	β-Mercaptoethanol
ET	Electron Transfer
MES	2-(N-morpholino) ethane sulfonic acid
TCEP	Tris(2-carboxyethyl) phosphine
ICP	Inductively Coupled Plasma
CD	Circular Dichroism spectroscopy
UV-Vis	Ultraviolet-Visible spectroscopy
MCD	Magnetic Circular Dichroism spectroscopy
NHE	Normal Hydrogen Electrode
HiPIP	High-potential iron-sulfur protein
NADH	Nicotinamide Adenine Dinucleotide Hydrogen
NADPH	Nicotinamide Adenine Dinucleotide Phosphate Hydrogen
METP	Miniaturized Electron Transfer Protein
EDT	Ethane-1,2-Dithiol
TIS	Triisopropylsilane

References

1. Lu Y, Yeung N, Sieracki N, Marshall NM. Design of functional metalloproteins. Nature [Internet] 2009 [cited 2023 Oct 1];460:855–62. Available from: https://www.nature.com/articles/nature08304

2. Atkins P. Shriver and Atkins' Inorganic Chemistry. OUP Oxford; 2010.

3. Lu Y, Berry SM, Pfister TD. Engineering Novel Metalloproteins: Design of Metal-Binding Sites into Native Protein Scaffolds. Chem. Rev. [Internet] 2001 [cited 2023 Oct 17];101:3047–80. Available from: https://doi.org/10.1021/cr0000574

4. Harding MM, Nowicki MW, Walkinshaw MD. Metals in protein structures: a review of their principal features. Crystallography Reviews [Internet] 2010;16:247–302. Available from: https://doi.org/10.1080/0889311X.2010.485616

5. Zhang SQ, Chino M, Liu L, Tang Y, Hu X, DeGrado WF, et al. De Novo Design of Tetranuclear Transition Metal Clusters Stabilized by Hydrogen-Bonded Networks in Helical Bundles. J. Am. Chem. Soc. [Internet] 2018 [cited 2024 Sep 6];140:1294–304. Available from: https://doi.org/10.1021/jacs.7b08261

6. Angela Lombardi VF. FUNCTIONAL CHARACTERIZATION OF SYNTHETIC METALLOPORPHYRINCONTAINING ENZYMES [Internet]. [cited 2024 Sep 6];Available from: http://www.fedoa.unina.it/12280/1/Vincenzo_Firpo_PhD_Thesis.pdf

7. Holm RH, Kennepohl P, Solomon EI. Structural and Functional Aspects of Metal Sites in Biology. Chem Rev 1996;96:2239–314.

8. Ohta T, Hagiwara Y, Kang J, Nishikawa K, Yamamoto T, Nagao H, et al. Evaluation of Electronic and Geometrical Properties of the Blue Copper Site in Fully Solvated Azurin by QM/MM Hybrid Calculations Using a New Interface Program Connecting QM and MM Engines. Journal of Computational and Theoretical Nanoscience 2009;6:2648–55.

9. Ciferri A, Perico A. Ionic Interactions in Natural and Synthetic Macromolecules | Wiley [Internet]. [cited 2023 Oct 3]. Available from: https://www.wiley.com/en-us/Ionic+Interactions+in+Natural+and+Synthetic+Macromolecules-p-9780470529270

10. D'Alonzo D, De Fenza M, Pavone V, Lombardi A, Nastri F. Selective Oxidation of Halophenols Catalyzed by an Artificial Miniaturized Peroxidase. International Journal of Molecular Sciences 2023;24:8058.

11. Kretsinger RH, Uversky VN, Permyakov EA. Encyclopedia of metalloproteins. Springer; 2013.

12. Bertini I, Gray HB, Lippard SJ, Valentine JS. Bioinorganic chemistry. University science books; 1994.

13. Nanda V, Koder RL. Designing artificial enzymes by intuition and computation. Nat Chem 2010;2:15–24.

14. Liu J, Chakraborty S, Hosseinzadeh P, Yu Y, Tian S, Petrik I, et al. Metalloproteins Containing Cytochrome, Iron–Sulfur, or Copper Redox Centers. Chem. Rev. [Internet] 2014;114:4366–469. Available from: https://doi.org/10.1021/cr400479b

15. Meyer J. Iron-sulfur protein folds, iron-sulfur chemistry, and evolution. J Biol Inorg Chem 2008;13:157–70.

16. Johnson DC, Dean DR, Smith AD, Johnson MK. Structure, function, and formation of biological iron-sulfur clusters. Annu Rev Biochem 2005;74:247–81.

17. Beinert H, Holm RH, Münck E. Iron-sulfur clusters: nature's modular, multipurpose structures. Science 1997;277:653–9.

18. Flint DH, Allen RM. Ironminus signSulfur Proteins with Nonredox Functions. Chem Rev 1996;96:2315–34.

19. Lill R. Function and biogenesis of iron-sulphur proteins. Nature 2009;460:831–8.

20. Meyer J. Iron–sulfur protein folds, iron–sulfur chemistry, and evolution. JBIC Journal of Biological Inorganic Chemistry 2008;13:157–70.

21. Jenney FE, Verhagen MF, Cui X, Adams MW. Anaerobic microbes: oxygen detoxification without superoxide dismutase. Science 1999;286:306–9.

22. Meyer J, Moulis J. Rubredoxin. Handbook of metalloproteins 2006;

23. Williams SC, Austin RN. An Overview of the Electron-Transfer Proteins That Activate Alkane Monooxygenase (AlkB). Frontiers in Microbiology [Internet] 2022 [cited 2024 Jan 4];13. Available from: https://www.frontiersin.org/articles/10.3389/fmicb.2022.845551

24. Lode ET, Coon MJ. Enzymatic ω-Oxidation: V. FORMS OF PSEUDOMONAS OLEOVORANS RUBREDOXIN CONTAINING ONE OR TWO IRON ATOMS: STRUCTURE AND FUNCTION IN ω-HYDROXYLATION. Journal of Biological Chemistry [Internet] 1971 [cited 2024 Jan 4];246:791–802. Available from: https://www.sciencedirect.com/science/article/pii/S0021925818624792

25. Gaillard J, Zhuang-Jackson H, Moulis JM. Nuclear-magnetic-resonance determination of the electron self-exchange rate constant of Clostridium pasteurianum rubredoxin. Eur J Biochem 1996;238:346–9.

26. Bragança PM da S. Incorporation of a Mo in a Rubredoxin-Type Centre of a de Novo Designed α3-DIV-L21C Three Helix Bundle Peptide [Internet]. 2019 [cited 2024 Sep 4];Available from: https://run.unl.pt/handle/10362/89462

27. Hiller R, Zhou ZH, Adams MWW, Englander SW. Stability and dynamics in a hyperthermophilic protein with melting temperature close to 200°C. Proceedings of

the National Academy of Sciences [Internet] 1997 [cited 2024 Jan 4];94:11329–32. Available from: https://www.pnas.org/doi/10.1073/pnas.94.21.11329

28. Wastl J, Duin EC, Iuzzolino L, Dörner W, Link T, Hoffmann S, et al. Eukaryotically encoded and chloroplast-located rubredoxin is associated with photosystem II. J Biol Chem 2000;275:30058–63.

29. Victor BL, Baptista AM, Soares CM. Dioxygen and nitric oxide pathways and affinity to the catalytic site of rubredoxin:oxygen oxidoreductase from Desulfovibrio gigas. J Biol Inorg Chem 2009;14:853–62.

30. Sieker LC, Stenkamp RE, LeGall J. Rubredoxin in crystalline state. Methods Enzymol 1994;243:203–16.

31. Vondrásek J, Bendová L, Klusák V, Hobza P. Unexpectedly strong energy stabilization inside the hydrophobic core of small protein rubredoxin mediated by aromatic residues: correlated ab initio quantum chemical calculations. J Am Chem Soc 2005;127:2615–9.

32. Perry A, Tambyrajah W, Grossmann JG, Lian LY, Scrutton NS. Solution structure of the two-iron rubredoxin of Pseudomonas oleovorans determined by NMR spectroscopy and solution X-ray scattering and interactions with rubredoxin reductase. Biochemistry 2004;43:3167–82.

33. Tunney JM, McMaster J, Garner CD. 8.18 - Molybdenum and Tungsten Enzymes [Internet]. In: McCleverty JA, Meyer TJ, editors. Comprehensive Coordination Chemistry II. Oxford: Pergamon; 2003 [cited 2023 Oct 15]. page 459–77.Available from: https://www.sciencedirect.com/science/article/pii/B0080437486081688

34. Bragança PMS, Carepo MSP, Pauleta SR, Pinter TBJ, Elia M, Cordas CM, et al. Incorporation of a molybdenum atom in a Rubredoxin-type Centre of a de novo-designed α3DIV-L21C three-helical bundle peptide. Journal of Inorganic Biochemistry [Internet] 2023 [cited 2023 May 5];240:112096. Available from: https://www.sciencedirect.com/science/article/pii/S0162013422003853

35. Slater JW, Marguet SC, Monaco HA, Shafaat HS. Going beyond Structure: Nickel-Substituted Rubredoxin as a Mechanistic Model for the [NiFe] Hydrogenases. J. Am. Chem. Soc. [Internet] 2018 [cited 2023 Oct 15];140:10250–62. Available from: https://doi.org/10.1021/jacs.8b05194

36. Slater JW, Shafaat HS. Nickel-Substituted Rubredoxin as a Minimal Enzyme Model for Hydrogenase. J Phys Chem Lett 2015;6:3731–6.

37. Maher M, Cross M, Wilce MCJ, Guss JM, Wedd AG. Metal-substituted derivatives of the rubredoxin from Clostridium pasteurianum. Acta Crystallogr D Biol Crystallogr 2004;60:298–303.

38. Thapper A, Rizzi AC, Brondino CD, Wedd AG, Pais RJ, Maiti BK, et al. Copper-substituted forms of the wild type and C42A variant of rubredoxin. J Inorg Biochem 2013;127:232–7.

39. Maiti BK, Maia LB, Moro AJ, Lima JC, Cordas CM, Moura I, et al. Unusual Reduction Mechanism of Copper in Cysteine-Rich Environment. Inorg. Chem. [Internet] 2018 [cited 2023 Oct 15];57:8078–88. Available from: https://doi.org/10.1021/acs.inorgchem.8b00121

40. Dauter Z, Wilson KS, Sieker LC, Moulis JM, Meyer J. Zinc- and iron-rubredoxins from Clostridium pasteurianum at atomic resolution: a high-precision model of a ZnS4 coordination unit in a protein. Proceedings of the National Academy of Sciences [Internet] 1996 [cited 2023 Oct 15];93:8836–40. Available from: https://www.pnas.org/doi/abs/10.1073/pnas.93.17.8836

41. Petillot Y, Forest E, Mathieu I, Meyer J, Moulis JM. Analysis, by electrospray ionization mass spectrometry, of several forms of Clostridium pasteurianum rubredoxin. Biochemical Journal [Internet] 1993 [cited 2023 Oct 15];296:657–61. Available from: https://doi.org/10.1042/bj2960657

42. Archer M, Carvalho A l., Teixeira S, Moura I, Moura J j. g., Rusnak F, et al. Structural studies by X-ray diffraction on metal substituted desulforedoxin, a rubredoxin-type protein. Protein Science [Internet] 1999 [cited 2023 Oct 15];8:1536–45. Available from: https://onlinelibrary.wiley.com/doi/abs/10.1110/ps.8.7.1536

43. LeMaster DM, Minnich M, Parsons PJ, Anderson JS, Hernández G. Tetrathiolate coordination of germanium(IV) in a protein active site. Journal of Inorganic Biochemistry [Internet] 2006 [cited 2023 Oct 15];100:1410–2. Available from: https://www.sciencedirect.com/science/article/pii/S0162013406001048

44. Maiti BK, Maia LB, Silveira CM, Todorovic S, Carreira C, Carepo MSP, et al. Incorporation of molybdenum in rubredoxin: models for mononuclear molybdenum enzymes. J Biol Inorg Chem [Internet] 2015 [cited 2023 May 15];20:821–9. Available from: https://doi.org/10.1007/s00775-015-1268-0

45. Conrads T, Hemann C, George GN, Pickering IJ, Prince RC, Hille R. The Active Site of Arsenite Oxidase from Alcaligenes faecalis. J. Am. Chem. Soc. [Internet] 2002 [cited 2023 Oct 15];124:11276–7. Available from: https://doi.org/10.1021/ja027684q

46. Zaballa ME, Abriata LA, Donaire A, Vila AJ. Flexibility of the metal-binding region in apo-cupredoxins. Proceedings of the National Academy of Sciences [Internet] 2012 [cited 2023 Oct 15];109:9254–9. Available from: https://www.pnas.org/doi/full/10.1073/pnas.1119460109

47. Maiti BK, Maia LB, Silveira CM, Todorovic S, Carreira C, Carepo MSP, et al. Incorporation of molybdenum in rubredoxin: models for mononuclear molybdenum enzymes. J Biol Inorg Chem [Internet] 2015 [cited 2023 Mar 13];20:821–9. Available from: https://doi.org/10.1007/s00775-015-1268-0

48. Mitchell PCH. Coordination compounds of molybdenum. Coordination Chemistry Reviews [Internet] 1966 [cited 2023 Oct 15];1:315–50. Available from: https://www.sciencedirect.com/science/article/pii/S0010854500801435

49. Zhang Y, Gladyshev VN. Molybdoproteomes and Evolution of Molybdenum Utilization. Journal of Molecular Biology [Internet] 2008 [cited 2023 Oct 15];379:881–99. Available from: https://www.sciencedirect.com/science/article/pii/S0022283608003823

50. Aguilar M, Kalakoutskii K, Cárdenas J, Fernández E. Direct transfer of molybdopterin cofactor to aponitrate reductase from a carrier protein in Chlamydomonas reinhardtii. FEBS Lett 1992;307:162–3.

51. Hagen WR. Cellular uptake of molybdenum and tungsten. Coordination Chemistry Reviews [Internet] 2011 [cited 2023 Oct 15];255:1117–28. Available from: https://www.sciencedirect.com/science/article/pii/S0010854511000671

52. Tejada-Jiménez M, Llamas Á, Sanz-Luque E, Galván A, Fernández E. A high-affinity molybdate transporter in eukaryotes. Proceedings of the National Academy of Sciences [Internet] 2007 [cited 2023 Oct 15];104:20126–30. Available from: https://www.pnas.org/doi/full/10.1073/pnas.0704646104

53. Biswas KC, Woodards NA, Xu H, Barton LL. Reduction of molybdate by sulfate-reducing bacteria. Biometals [Internet] 2009 [cited 2023 Oct 15];22:131–9. Available from: https://doi.org/10.1007/s10534-008-9198-8

54. Williams RJP, Fraústo da Silva JJR. The Involvement of Molybdenum in Life. Biochemical and Biophysical Research Communications [Internet] 2002 [cited 2023 Oct 15];292:293–9. Available from: https://www.sciencedirect.com/science/article/pii/S0006291X02965186

55. Wang D. Redox chemistry of molybdenum in natural waters and its involvement in biological evolution. Frontiers in Microbiology [Internet] 2012 [cited 2023 Oct 15];3. Available from: https://www.frontiersin.org/articles/10.3389/fmicb.2012.00427

56. Mendel RR. Molybdenum: biological activity and metabolism. Dalton Trans. [Internet] 2005 [cited 2023 Oct 15];3404–9. Available from: https://pubs.rsc.org/en/content/articlelanding/2005/dt/b505527j

57. Sigel A, Sigel H. Metal Ions in Biological Systems, Volume 35: Iron Transport and Storage Microorganisms, Plants, and Animals. Metal-Based Drugs [Internet] NaN/NaN/NaN [cited 2023 Oct 15];5:262–262. Available from: https://www.hindawi.com/journals/mbd/1998/359826/

58. Basu P, Burgmayer SJN. Recent developments in the study of molybdoenzyme models. J Biol Inorg Chem [Internet] 2015 [cited 2023 Oct 15];20:373–83. Available from: https://doi.org/10.1007/s00775-014-1228-0

59. Rivas MG, Carepo MSP, Mota CS, Korbas M, Durand MC, Lopes AT, et al. Molybdenum Induces the Expression of a Protein Containing a New Heterometallic Mo-Fe Cluster in Desulfovibrio alaskensis. Biochemistry [Internet] 2009 [cited 2023 Oct 15];48:873–82. Available from: https://doi.org/10.1021/bi801773t

60. Iobbi-Nivol C, Leimkühler S. Molybdenum enzymes, their maturation and molybdenum cofactor biosynthesis in Escherichia coli. Biochimica et Biophysica Acta (BBA) - Bioenergetics [Internet] 2013 [cited 2023 Oct 15];1827:1086–101. Available from: https://www.sciencedirect.com/science/article/pii/S0005272812010821

61. Moura JJG, Moura I, Maia LB, editors. Enzymes for Solving Humankind's Problems: Natural and Artificial Systems in Health, Agriculture, Environment and Energy [Internet]. Cham: Springer International Publishing; 2021 [cited 2024 Oct 25]. Available from: https://link.springer.com/10.1007/978-3-030-58315-6

62. Hille R. The Mononuclear Molybdenum Enzymes. Chem. Rev. [Internet] 1996 [cited 2023 May 15];96:2757–816. Available from: https://pubs.acs.org/doi/10.1021/cr950061t

63. Hille R. The Mononuclear Molybdenum Enzymes. Chem. Rev. [Internet] 1996 [cited 2024 Oct 25];96:2757–816. Available from: https://doi.org/10.1021/cr950061t

64. Rajapakshe A, Snyder RA, Astashkin AV, Bernardson P, Evans DJ, Young CG, et al. Insights into the nature of Mo(V) species in solution: Modeling catalytic cycles for molybdenum enzymes. Inorganica Chimica Acta [Internet] 2009 [cited 2023 Oct 15];362:4603–8. Available from: https://www.sciencedirect.com/science/article/pii/S002016930900320X

65. Hoffman BM, Lukoyanov D, Yang ZY, Dean DR, Seefeldt LC. Mechanism of Nitrogen Fixation by Nitrogenase: The Next Stage. Chem. Rev. [Internet] 2014 [cited 2023 Oct 15];114:4041–62. Available from: https://doi.org/10.1021/cr400641x

66. Rees DC, Akif Tezcan F, Haynes CA, Walton MY, Andrade S, Einsle O, et al. Structural basis of biological nitrogen fixation. Philosophical Transactions of the Royal Society A: Mathematical, Physical and Engineering Sciences [Internet] 2005 [cited 2023 Oct 15];363:971–84. Available from: https://royalsocietypublishing.org/doi/10.1098/rsta.2004.1539

67. Penning TM, Jez JM. Enzyme Redesign. Chem. Rev. [Internet] 2001 [cited 2023 Oct 17];101:3027–46. Available from: https://doi.org/10.1021/cr000049n

68. Corinne Cerrone. ARTIFICIAL HEME-ENZYMES FOR CATALYTIC AND DIAGNOSTIC APPLICATIONS [Internet]. [cited 2024 Sep 3];Available from: http://www.fedoa.unina.it/10513/1/Corinne%20Cerrone_PhD%20Thesis.pdf

69. Lu Y, Yeung N, Sieracki N, Marshall NM. Design of functional metalloproteins. Nature 2009;460:855–62.

70. Lombardi A, Marasco D, Maglio O, Di Costanzo L, Nastri F, Pavone V. Miniaturized metalloproteins: Application to iron–sulfur proteins. Proceedings of the National Academy of Sciences [Internet] 2000 [cited 2023 Oct 17];97:11922–7. Available from: https://www.pnas.org/doi/10.1073/pnas.97.22.11922

71. DeGrado WF, Summa CM, Pavone V, Nastri F, Lombardi A. De novo design and structural characterization of proteins and metalloproteins. Annu Rev Biochem 1999;68:779–819.

72. Lombardi A, Nastri F, Sanseverino M, Maglio O, Pedone C, Pavone V. Miniaturized hemoproteins: design, synthesis and characterization of mimochrome II. Inorganica Chimica Acta [Internet] 1998 [cited 2023 Oct 17];275–276:301–13. Available from: https://www.sciencedirect.com/science/article/pii/S002016939706180X

73. Sugimoto H, Tsukube H. Chemical analogues relevant to molybdenum and tungsten enzyme reaction centres toward structural dynamics and reaction diversity. Chem. Soc. Rev. [Internet] 2008 [cited 2023 Oct 15];37:2609–19. Available from: https://pubs.rsc.org/en/content/articlelanding/2008/cs/b610235m

74. Brondino CD, Romão MJ, Moura I, Moura JJ. Molybdenum and tungsten enzymes: the xanthine oxidase family. Current Opinion in Chemical Biology [Internet] 2006 [cited 2023 Oct 15];10:109–14. Available from: https://www.sciencedirect.com/science/article/pii/S1367593106000251

75. Wang JJ, Kryatova OP, Rybak-Akimova EV, Holm RH. Comparative Kinetics and Mechanism of Oxygen and Sulfur Atom Transfer Reactions Mediated by Bis(dithiolene) Complexes of Molybdenum and Tungsten. Inorg. Chem. [Internet] 2004 [cited 2023 Oct 15];43:8092–101. Available from: https://doi.org/10.1021/ic040087f

76. Pavone V, Gaeta G, Lombardi A, Nastri F, Maglio O, Isernia C, et al. Discovering protein secondary structures: classification and description of isolated alpha-turns. Biopolymers 1996;38:705–21.

77. HILL RB, RALEIGH DP, LOMBARDI A, DEGRADO WF. De Novo Design of Helical Bundles as Models for Understanding Protein Folding and Function. Acc Chem Res [Internet] 2000 [cited 2023 Oct 17];33:745–54. Available from: https://www.ncbi.nlm.nih.gov/pmc/articles/PMC3050006/

78. Leone L, Chino M, Nastri F, Maglio O, Pavone V, Lombardi A. Mimochrome, a metalloporphyrin-based catalytic Swiss knife†. Biotechnol Appl Biochem 2020;67:495–515.

79. Leone L, D'Alonzo D, Balland V, Zambrano G, Chino M, Nastri F, et al. Mn-Mimochrome VI*a: An Artificial Metalloenzyme With Peroxygenase Activity. Frontiers in Chemistry [Internet] 2018 [cited 2023 Oct 17];6. Available from: https://www.frontiersin.org/articles/10.3389/fchem.2018.00590

80. La Gatta S, Leone L, Maglio O, De Fenza M, Nastri F, Pavone V, et al. Unravelling the Structure of the Tetrahedral Metal-Binding Site in METP3 through an Experimental and Computational Approach. Molecules [Internet] 2021 [cited 2023 Oct 3];26:5221. Available from: https://www.mdpi.com/1420-3049/26/17/5221

81. Summa CM, Rosenblatt MM, Hong JK, Lear JD, DeGrado WF. Computational de novo design, and characterization of an A(2)B(2) diiron protein. J Mol Biol 2002;321:923–38.

82. Lombardi A, Marasco D, Maglio O, Di Costanzo L, Nastri F, Pavone V. Miniaturized metalloproteins: Application to iron–sulfur proteins. Proceedings of the National Academy of Sciences [Internet] 2000 [cited 2024 Sep 3];97:11922–7. Available from: https://www.pnas.org/doi/full/10.1073/pnas.97.22.11922

83. Chino M, Di Costanzo LF, Leone L, La Gatta S, Famulari A, Chiesa M, et al. Designed Rubredoxin miniature in a fully artificial electron chain triggered by visible light. Nat Commun [Internet] 2023 [cited 2023 Oct 17];14:2368. Available from: https://www.nature.com/articles/s41467-023-37941-8

84. Chino M, Leone L, Maglio O, D'Alonzo D, Pirro F, Pavone V, et al. A De Novo Heterodimeric Due Ferri Protein Minimizes the Release of Reactive Intermediates in Dioxygen-Dependent Oxidation. Angew Chem Int Ed Engl 2017;56:15580–3.

85. Nanda V, Rosenblatt MM, Osyczka A, Kono H, Getahun Z, Dutton PL, et al. De novo design of a redox-active minimal rubredoxin mimic. J Am Chem Soc 2005;127:5804–5.

86. Eidsness MK, Burden AE, Richie KA, Kurtz DM, Scott RA, Smith ET, et al. Modulation of the redox potential of the [Fe(SCys)(4)] site in rubredoxin by the orientation of a peptide dipole. Biochemistry 1999;38:14803–9.

87. Chou PY, Fasman GD. Beta-turns in proteins. J Mol Biol 1977;115:135–75.

88. Spence J, Chang HH. Complexes of Cysteine with Molybdenum (V) and Molybdenum (VI). Inorganic Chemistry 1963;2:319–23.

89. Buchanan I, Minelli M, Ashby MT, King TJ, Enemark JH, Garner CD. Crystal structure and spectroscopic studies of [MoO2 (L-Cys-OMe) 2]. Inorganic Chemistry 1984;23:495–500.

90. Bishop PT, Dilworth JR, Hutchinson JP, Zubieta JA. Syntheses and x-ray crystal structures of [MoO (SCH2CH2-CH2S) 2]− and [Mo2O2 (μ-N3)(SCH2CH2CH2S) 3]−. A study of the redox behaviour of [MoO (SCH2CH2S) 2]− by cyclic voltammetry using convolution analysis. Transition Metal Chemistry 1990;15:177–82.

91. Huang TJ, Haight Jr GP. Paramagnetic monomeric molybdenum (V)-cysteine complex as a model for molybdenum-enzyme interaction. Journal of the American Chemical Society 1970;92:2336–42.

92. Ueyama N, Okamura T, Nakamura A. Structure and properties of molybdenum (IV, V) arenethiolates with a neighboring amide group. Significant contribution of NH. cntdot.. cntdot.. cntdot. S hydrogen bond to the positive shift of redox potential of Mo (V)/Mo (IV). Journal of the American Chemical Society 1992;114:8129–37.

93. Junkers M. ChemMatrix® Resin–A major advance in solid phase peptide synthesis. Aldrich ChemFiles 2011;11:10–2.

94. Cn P, F V, L F, G G, T G. How to measure and predict the molar absorption coefficient of a protein. Protein science□: a publication of the Protein Society [Internet] 1995 [cited 2023 Nov 22];4. Available from: https://pubmed.ncbi.nlm.nih.gov/8563639/

95. Spence J, Chang HH. Complexes of Cysteine with Molybdenum (V) and Molybdenum (VI). Inorganic Chemistry 1963;2:319–23.

96. Quagraine EK, Reid RS. UV/visible spectrophotometric studies of the interactions of thiomolybdates, copper(II) and other ligands. J Inorg Biochem 2001;85:53–60.

97. Laurie SH. Thiomolybdates — Simple but Very Versatile Reagents. European Journal of Inorganic Chemistry [Internet] 2000 [cited 2023 Nov 26];2000:2443–50. Available from: https://onlinelibrary.wiley.com/doi/abs/10.1002/1099-0682%28200012%292000%3A12%3C2443%3A%3AAID-EJIC2443%3E3.0.CO%3B2-I

98. Huang TJ, Haight Jr GP. Paramagnetic monomeric molybdenum (V)-cysteine complex as a model for molybdenum-enzyme interaction. Journal of the American Chemical Society 1970;92:2336–42.

99. Buchanan I, Minelli M, Ashby MT, King TJ, Enemark JH, Garner CD. Crystal structure and spectroscopic studies of [MoO2 (L-Cys-OMe) 2]. Inorganic Chemistry 1984;23:495–500.

100. Bishop PT, Dilworth JR, Hutchinson JP, Zubieta JA. Syntheses and x-ray crystal structures of [MoO (SCH2CH2-CH2S) 2]− and [Mo2O2 (μ-N3)(SCH2CH2CH2S) 3]−. A study of the redox behaviour of [MoO (SCH2CH2S) 2]− by cyclic voltammetry using convolution analysis. Transition Metal Chemistry 1990;15:177–82.

101. Maiti BK, Maia LB, Silveira CM, Todorovic S, Carreira C, Carepo MSP, et al. Incorporation of molybdenum in rubredoxin: models for mononuclear molybdenum enzymes. JBIC Journal of Biological Inorganic Chemistry [Internet] 2015;20:821–9. Available from: https://doi.org/10.1007/s00775-015-1268-0

102. Woody RW. Theory of circular dichroism of proteins. In: Circular dichroism and the conformational analysis of biomolecules. Springer; 1996. page 25–67.

103. Greenfield NJ. Using circular dichroism spectra to estimate protein secondary structure. Nat Protoc [Internet] 2006 [cited 2023 Nov 30];1:2876–90. Available from: https://www.ncbi.nlm.nih.gov/pmc/articles/PMC2728378/

Appendices

Appendix A

Supporting Information

Figure S1

Stereo View of Val5-Glu12 and Val39-Pro45 from DvRd as a Ribbon Diagram with Indicated C_2 Symmetry Axis

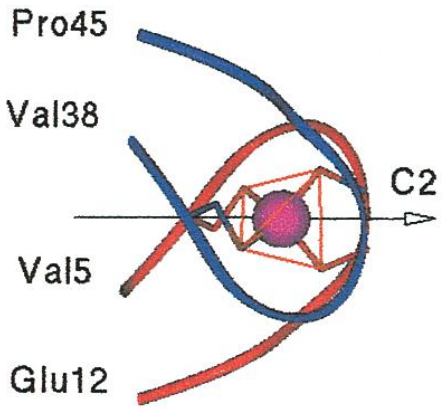

Figure S2

Symmetric Dimer Reconstruction from Cys-$(X)_2$-Cys-X Pentapeptide Using Productive C2 Symmetry Axes: A) Λ Isomer via b Axis; B) Unproductive a Symmetry Axis; C) Δ Isomer via c Axis.

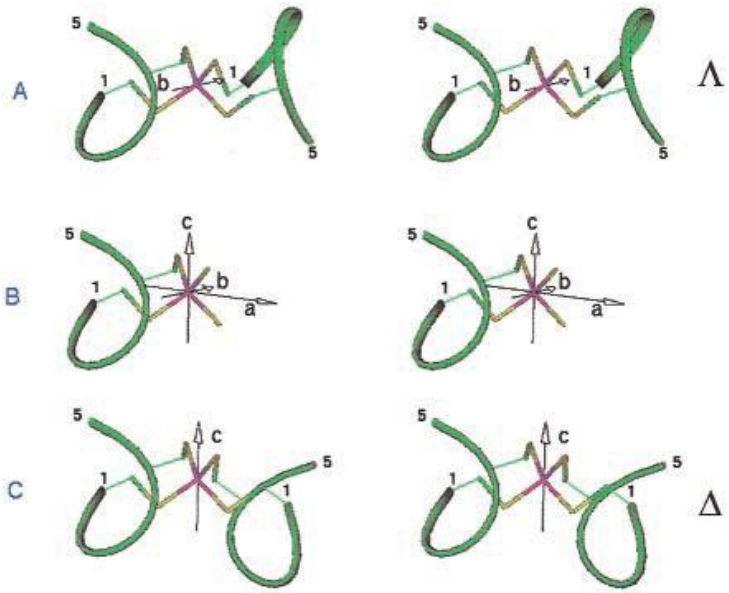

Figure S3

Zn(II)-METPsc1 Structural Characterization.

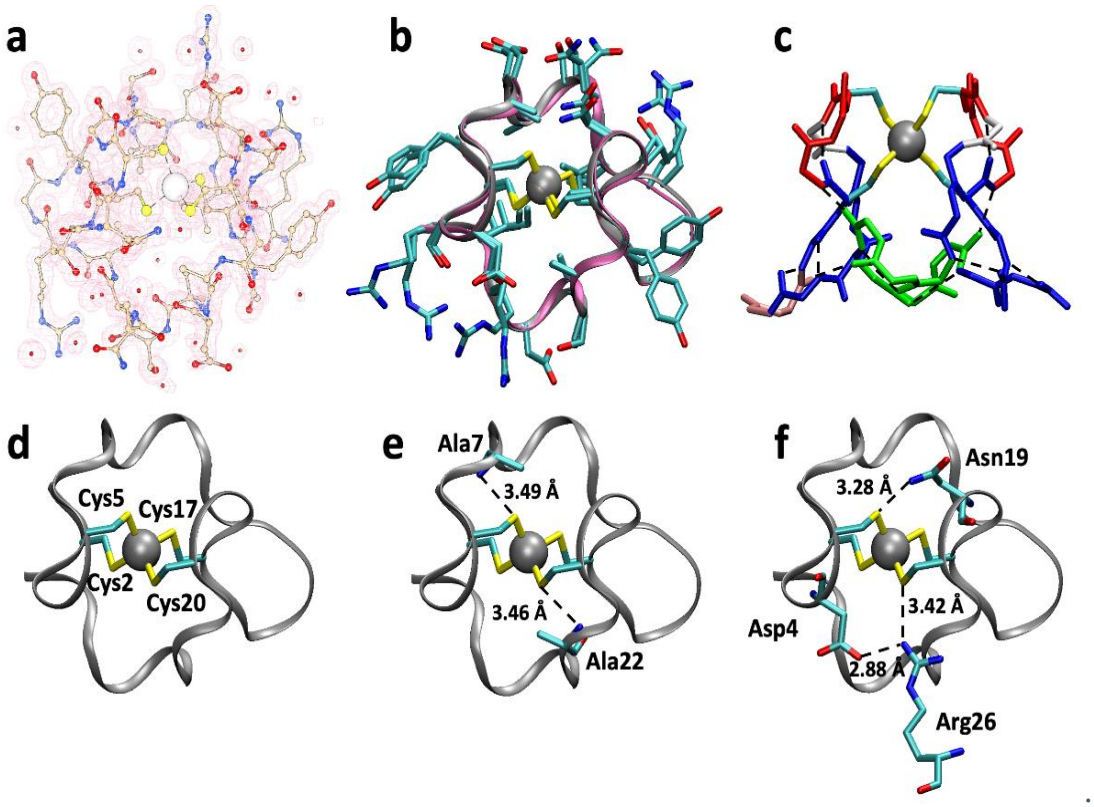

a) The electron density map showing the metal ion, all side chains, and N- and C-terminal capping groups. b) The monomeric X-ray structure of Zn(II)-METPsc1 (cyan) aligns with the designed model (light brown). C) Secondary structural elements in Zn(II)-METPsc1: β-strand (blue), α-turn (red), β-bulge (gray), 310-helix (green), and type I' β-turn (orange). Dashed lines indicate hydrogen bonds. d) The first coordination sphere, highlighting the coordination bond between zinc and cysteine sulfur atoms. e) The second coordination sphere, showing hydrogen bonds between the backbone amides of Ala7 and Ala22 to sulfur atoms. f) Hydrogen bond donors from the side chains of Asn19 and a symmetry-related Arg26 (cyan) to METPsc1 partners.

Table S1

Chemical structures for the materials

2-Mercaptoethanol (β-ME)	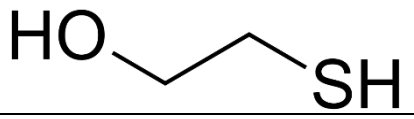
Sodium molybdate	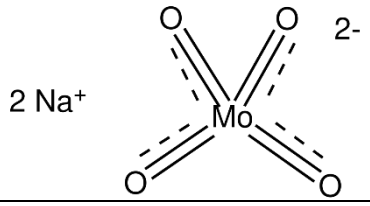
2-Morpholinoethanesulfonic acid monohydrate	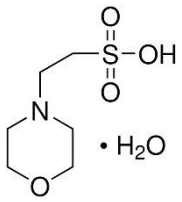
Acetonitrile	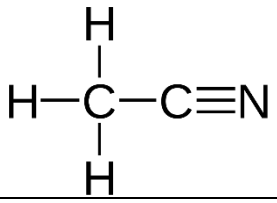
Trifluoroacetic acid	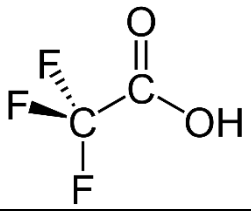
Hydrochloric acid	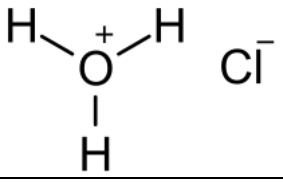

جامعة النجاح الوطنية
كلية الدراسات العليا

التوصيف الطيفي الكيميائي لسقالة بروتين مصغرة لنقل الإلكترون تحاكي موقع معدن الروبريدوكسين: ال موليبدينوم – سلسلة بروتين نقل الإلكترون المصغرة 1 (Mo-METPsc1)

إعداد
رفيف محمد عبد المجيد عدوان

إشراف
د. ضياء عارف
د. محمد سليمان

قدمت هذه الرسالة استكمالا لمتطلبات الحصول على درجة الماجستير في الكيمياء،
من كلية الدراسات العليا، في جامعة النجاح الوطنية، نابلس – فلسطين.

2024

التوصيف الطيفي الكيميائي لسقالة بروتين مصغرة لنقل الإلكترون تحاكي موقع معدن الروبريدوكسين: ال موليبدينوم – سلسلة بروتين نقل الإلكترون المصغرة 1 (Mo-METPsc1)

إعداد

رفيف محمد عبد المجيد عدوان

إشراف

د. ضياء عارف

د. محمد سليمان

الملخص

الذرات المعدنية أســـاســـية في التحفيز وهي جزء لا يتجزأ من بنية ووظيفة العديد من الإنزيمات والبروتينات. يتمثل الهدف الرئيسي في تصميم البروتينات في تطوير هياكل ببتيدية صغيرة ومستقرة وبسيطة يمكنها محاكاة النشـــاط التحفيزي لمراكز المعادن المعقدة في البروتينات. هذه النماذج الاصـــطناعية لديها إمكانات كبيرة في مجالات مثل التطبيقات البيئية، التكنولوجيا الحيوية، والأبحاث الأساسية.

في هذه الدراسة، ركزنا على الببتيد أحادي السلسلة البروتيني المصغر لنقل الإلكترونات (METPsc1)، الذي تم إعادة تكوينه لمحاكاة موقع ارتباط معدني يـ شبه الروبريدوك سين ببيئة ثيول رباعية دقيقة. تم تحقيق إعادة تكوين ببتيد الموليبدينوم أحادي السلسلة المصغر لنقل الإلكترونات 1 (Mo-METPsc1) باستخدام نسب مختلفة من الببتيد إلى المعدن، وتمت دراسة التركيب باستخدام تقنيات طيفية متعددة، بما في ذلك الأشعة فوق البنفسجية المرئية (UV-vis)، والاستقطاب الدائري (CD)، والاستقطاب الدائري المغناطيسي (MCD).

حددت تقنية الأشعة فوق البنفسجية المرئية نطاقي امتصاص واسعَين، مع قمم بين 310–330 نانومتر و420–460 نانومتر، مما يدل على النجاح في دمج الموليبدينوم في بيئة رباعية الثيول. وأكدت تقنية الاستقطاب الدائري (CD) ارتباط الموليبدينوم، حيث أظهرت نطاقًا إيجابيًا عند 394 نانومتر. كشـــفت تقنية الاســـتقطاب الدائري المغناطيسي (MCD)، التي تكون حساسة للبنية الإلكترونية وحالة الأكسدة، أن الموليبدينوم في موقع ارتباط المعدن في حالة الأكسدة 6^+ (Mo (VI)).

تؤكد هذه التحليلات الطيفية نجاح دمج الموليبدينوم ووظيفته ضـــمن الهيكل الببتيدي. وللتحقق من قدرة مركب Mo-METPsc1 على الاختزال، تم إجراء درا سات با ستخدام مادة ثيو سلفات وثيول ثنائي الريبيتول كركائز. أظهرت التحليلات الطيفية بعد هذه الاختبارات النشاط التحفيزي للمركب في اختزال جزيء الثيوسلفات.

الكلمات المفتاحية: روبريدوكســـين، METPsc1، ببتيدات معدنية صـــطناعية، ببتيدات مرتبطة بالموليبدينوم، التحفيز البيولوجي.